Weakly linked binary mixtures of $F = 1$ ^{87}Rb Bose–Einstein condensates

Weakly linked binary mixtures of $F = 1$ ^{87}Rb Bose–Einstein condensates

M Melé-Messeguer[1,5]**, B Juliá-Díaz**[1,2]**, M Guilleumas**[1]**, A Polls**[1,2] **and A Sanpera**[3,4]

[1] Departament d'Estructura i Constituents de la Matèria, Facultat de Física, Universitat de Barcelona, E-08028, Barcelona, Spain
[2] Institut de Ciències del Cosmos, Universitat de Barcelona, E-08028 Barcelona, Spain
[3] ICREA-Institució Catalana de Recerca i Estudis Avançats, Lluís Companys 23, E-08010 Barcelona, Spain
[4] Grup de Física Teòrica: Informació i Processos Quàntics, Universitat Autònoma de Barcelona, E-08193 Bellaterra, Spain
E-mail: marina@ecm.ub.es

Abstract. We present a study of binary mixtures of Bose–Einstein condensates confined in a double-well potential within the framework of the mean field Gross–Pitaevskii (GP) equation. We re-examine both the single component and the binary mixture cases for such a potential, and we investigate what are the situations in which a simpler two-mode approach leads to an accurate description of their dynamics. We also estimate the validity of the most usual dimensionality reductions used to solve the GP equations. To this end, we compare both the semi-analytical two-mode approaches and the numerical simulations of the one-dimensional (1D) reductions with the full 3D numerical solutions of the GP equation. Our analysis provides a guide to clarify the validity of several simplified models that describe mean-field nonlinear dynamics, using an experimentally feasible binary mixture of an $F = 1$ spinor condensate with two of its Zeeman manifolds populated, $m = \pm 1$.

[5] Author to whom any correspondence should be addressed.

IOP Institute of Physics Φ DEUTSCHE PHYSIKALISCHE GESELLSCHAFT

Contents

1. Introduction

The phase coherence of a Bose–Einstein condensate (BEC) is an important and characteristic property of ultracold bosonic gases that leads to fascinating macroscopic phenomena such as interference effects or Josephson-type oscillations. Two condensates trapped in a double-well potential exhibit interference fringes when the barrier is released and the two expanding condensates, with a well-defined quantum phase, overlap. Instead, if the barrier is not switched off and is large enough to ensure a weak link between both condensates on each side of the trap, the quantum phase difference will drive Josephson-like effects, which consist of fast oscillating tunneling, much faster than single particle tunneling, of atoms through the potential barrier [1, 2].

The first evidence of the phase coherence of a BEC was obtained in early interference experiments [3], where clean interference patterns appeared in the overlapping region of two expanding condensates. It is only recently that clear evidence of an external bosonic Josephson junction in a weakly linked scalar BEC[6] has been experimentally reported, first by the group of

---

[6] The notation 'scalar BEC' is used as the equivalent of 'single-component BEC' in this paper.

M Oberthaler in Heidelberg [4], followed by the group of J Steinhauer [5]. Internal Josephson dynamics has also been reported experimentally in [6].

In the experiment of [4], two condensates are confined in a double-well potential with an initial population imbalance between both sides that triggers the Josephson oscillations. The tunneling of particles leads to a coupled dynamical evolution of the two conjugate variables, the phase difference between the two weakly linked condensates and their population imbalance. In spite of the system being very dilute, the inter-species interaction plays a crucial role in the Josephson dynamics, leading to new regimes beyond the standard Josephson effect, e.g. macroscopic quantum self-trapping (MQST).

The Gross–Pitaevskii (GP) mean-field theory provides a well-grounded framework for investigating Josephson dynamics in weakly interacting systems provided that (a) the number of atoms is large enough so that quantum fluctuations can be neglected and (b) the initial many-body state is of mean-field type. Josephson oscillations in scalar BECs have been theoretically studied by using different techniques [7]–[12], [13]–[24]. For a small number of atoms, $N \lesssim 100$, the exact Josephson dynamics obtained by solving the corresponding many-body Schrödinger equation has been recently shown to depart from the mean-field GP, as clearly seen in the evolution of population imbalance or with the appearance of fragmentation [20]. For small N the transition from Josephson to self-trapped dynamics has also been shown, by analyzing a many-body Bose–Hubbard, to involve the appearance of strongly correlated quantum states [21].

For larger numbers of atoms, $N \gtrsim 1000$, however, the quantum fluctuations involving strongly correlated quantum states or fragmentation of the condensate are severely diminished. Thus, the full three-dimensional (3D) time-dependent Gross–Pitaevskii equation (GP3D) shows reasonable agreement with the experimental data of [4], [14, 15, 25], where $N \sim 1150$ and the system is allowed to evolve for less than a Rabi time.

However, since 3D dynamics need, in general, rather involved calculations, one can benefit from the fact that the barrier is created along one direction and the tunneling of particles is mainly 1D to investigate the Josephson dynamics by means of effective 1D GP-like equations. Among these reduced GP equations, the non-polynomial nonlinear Schrödinger equation (NPSE) proposed in [26] has shown the best agreement with the experimental results on scalar condensates [25], whereas another effective 1D Gross–Pitaevskii equation (GP1D) fails to describe the dynamics for a large number of trapped atoms in the same trapping conditions as in the Heidelberg experiment [15, 25].

Interactions are important for understanding the different regimes of the tunneling dynamics. Therefore, multi-component BECs in double-well potentials offer an interesting extension to study phenomena related to phase coherence. In particular, the Josephson dynamics will become richer due to the interplay between intra- and inter-species interactions.

Josephson oscillations in binary mixtures confined in double-well potentials have been addressed in a number of recent papers. The case of two-component BECs with density–density interactions has been studied within two-mode approaches in [27]–[35]. The papers [31, 34] go one step further and also consider GP1D simulations. Spin-dependent interactions have been addressed in [36, 37]. The Josephson dynamics in spinor condensates confined in double wells, characterized by an exchange of population between different Zeeman components, has also been investigated in [38, 39]. In [31, 36], the relevance of studying Josephson dynamics in binary mixtures has been emphasized, as it can give one access to information about the different scattering lengths present in the system.

Recently, the equations for the tunneling dynamics in a binary mixture within the two-mode approximation to the GP equations were derived in [30]. However, the authors have not compared their two-mode analysis with direct numerical resolutions of the GP equation, and have also not provided microscopic values to the parameters of the two-mode equations. Their main result is the description of a symmetry breaking pattern occurring when the inter- and intra-species interactions differ substantially. In [31], a comparison of the standard two-mode approach and the coupled GP1D equations for the mixture has been presented for one specific double-well potential that allows an analytical treatment.

For single component BECs, the range of validity of the different approximations to the Josephson dynamics has already been studied comparing with GP3D calculations and with the experimental results. However, no comparison with the full GP3D dynamics has been so far performed for a binary mixture in a double-well potential.

The aim of this paper is to investigate systematically the tunneling dynamics of a binary mixture of BECs trapped in a double-well potential, as well as the validity of the different mean-field approximations. We consider a mixture of two components obtained by populating two Zeeman states of an $F = 1$ ^{87}Rb condensate confined in the same double-well potential as in the experiments [4]. This system corresponds to a natural extension of the experimental work of [4], where only one of the Zeeman components was populated.

We provide a general overview of the different techniques used to investigate Josephson dynamics within the two-mode model (standard and improved two-mode) and within the GP framework (1D reductions of the GP equation, GP1D and NPSE). To this end, we solve the full 3D time-dependent GP equation for the mixture as a reference to assess and analyze the validity of the previous approximations.

This paper is organized as follows. The general framework of the coupled GP equations for a binary mixture is presented in section 2. In section 3, we derive analytic two-mode models both for single and two-component systems. First we recall the standard two-mode model (S2M). Then we derive the equations of the improved two-mode model (I2M) for a binary mixture, generalizing the work for a single component BEC performed in [14]. We discuss the stability of the dynamical equations and look for the stationary points for a binary mixture. In section 4, we analyze the different 1D reductions of the GP3D equations for the mixture: GP1D and NPSE. In section 5, we revisit the dynamics of a single component condensate in a double-well potential with the same parameters as in the experiment [4]. The tunneling dynamics in two-component systems is accurately discussed in section 6. We obtain the dynamics by solving the coupled GP3D equations for the mixture and show that for certain conditions there exists good agreement between I2M and GP3D, as well as for NPSE and GP3D. The range of validity of the two-mode models is explored paying special attention to situations that fall beyond the two-mode approximation. Finally, we discuss the cases that present characteristic features arising from the mixture, with no analogue in the tunneling dynamics of a single component BEC. The conclusions are presented in section 7.

2. Mean field approach: Gross–Pitaevskii (GP) equations

We consider a binary mixture of weakly interacting atoms at zero temperature, confined by the same double-well potential, $V(\mathbf{r})$. For dilute systems with a sufficiently large number of particles, the GP equation provides a suitable framework for studying the dynamics. In the mean field approximation, each condensate is described by the corresponding wave function

$\Psi_i(\mathbf{r}; t)$, with $i = a, b$ denoting each of the two components of the binary mixture. To avoid any misunderstanding, let us remind the reader that we are describing two different kinds of atoms, a and b, which evolve on a double-well external potential. In most situations, the system will behave as if there were four weakly linked Bose–Einstein condensates, two per component of the binary mixture per side of the potential barrier. The mean field description will reflect this feature by the homogeneous quantum phase of $\Psi_i(\mathbf{r}; t)$ at each side of the potential barrier, as will be discussed in great detail in the following sections.

The dynamical evolution of the two wave functions can be obtained by solving the two coupled GP equations:

$$i\hbar\frac{\partial\Psi_a(\mathbf{r}; t)}{\partial t} = \left[-\frac{\hbar^2}{2m_a}\nabla^2 + V(\mathbf{r}) + g_{aa}N_a|\Psi_a(\mathbf{r}; t)|^2 + g_{ab}N_b|\Psi_b(\mathbf{r}; t)|^2 \right] \Psi_a(\mathbf{r}; t),$$

$$i\hbar\frac{\partial\Psi_b(\mathbf{r}; t)}{\partial t} = \left[-\frac{\hbar^2}{2m_b}\nabla^2 + V(\mathbf{r}) + g_{ba}N_a|\Psi_a(\mathbf{r}; t)|^2 + g_{bb}N_b|\Psi_b(\mathbf{r}; t)|^2 \right] \Psi_b(\mathbf{r}; t).$$

$$(1)$$

For each component, the condensate wave function $\Psi_i(\mathbf{r}; t)$ is normalized to 1, m_i is the atomic mass, and $g_{ii} = 4\pi\hbar^2 a_i/m_i$ is the effective atomic interaction between atoms of the same species, with a_i being the corresponding s-wave scattering length. The coupling between both components is governed by the inter-species interaction $g_{ab} \equiv g_{ba}$, which depends on the specific nature of the binary mixture. The total number of atoms in the mixture is $N = N_a + N_b$.

There are many experimental possibilities to study the dynamics of binary mixtures of BECs. We will restrict our study to one of them, which is experimentally feasible. We will consider binary mixtures made of $F = 1$ ^{87}Rb atoms populating the $m = \pm 1$ Zeeman sublevels [40]. This implementation greatly simplifies the dynamics as the inter- and intra-species couplings are very similar in magnitude. Of course this choice limits the phenomena that can be observed; for example, the interesting symmetry breaking pattern discussed in [30], which relies on the inter-species coupling being larger than the intra-species one, will not take place; see section 6.5.

On the other hand, its simplicity allows us to discuss in detail the different approaches taken in the literature, e.g. two-mode models of the GP equations, 1D reductions, etc. As occurred in the scalar case, the dynamical features contained in equations (1) can, to a large extent, be described by a simplified two-mode model for each component. In the next section, we follow [7], [14] and [30] and derive two-mode expressions for the scalar and binary cases. The usual assumption of neglecting the overlaps involving the right and left modes gives rise to the so-called standard two-mode (S2M) equations; while retaining them one also gets a closed system of equations, the improved two-mode (I2M). Both the S2M and I2M are also derived for the binary mixture case.

3. Two-mode approaches

The two-mode approximation allows us to study the dynamics of weakly linked Bose–Einstein condensates without solving the full GP3D and without reducing the dimensionality of the GP equation [7, 14]. Depending on the specific double-well potential, e.g. on the energy gap between the first two levels of the single particle Hamiltonian and the next two, it can provide an excellent description of the full GP solution. The relevant physical quantity is the ratio between the energy gap between the ground state and first excited state of the double-well

potential, $\delta E_{0;1} = E_1 - E_0$,[7] and the energy difference of the ground state and the second excited state, $\delta E_{0;2} = E_2 - E_0$. Within the limits of applicability of the GP, a small ratio $\delta E_{0;1}/\delta E_{0;2}$ indicates that the second excited state will not play a role in the dynamics and thus the two-mode approach will be accurate[8]. The two-mode description characterizes the dynamics of the scalar condensate in a double-well potential with only two variables: the relative population and the phase difference between the left and right sides of the potential barrier.

3.1. Standard two-mode model for the single component case

The GP equation for the scalar case corresponds to a particular limit of the GP equations for the binary mixture, equations (1),

$$i\hbar \frac{\partial \Psi(\mathbf{r};t)}{\partial t} = \left[-\frac{\hbar^2}{2m}\nabla^2 + V(\mathbf{r}) + gN|\Psi(\mathbf{r};t)|^2 \right] \Psi(\mathbf{r};t). \tag{2}$$

We will make use of the following notation: $H_0 = -(\hbar^2/2m)\nabla^2 + V(\mathbf{r})$, and $H_g[\Psi] = gN|\Psi(\mathbf{r};t)|^2$. Let us recall the two-mode approximation for a single component condensate in a double-well potential. We consider N interacting atoms with atomic mass m, and coupling constant g, trapped in a symmetric double-well potential $V(\mathbf{r})$. When both sides of the potential barrier are weakly linked, the total wave function can be approximately written as a superposition of two time-independent spatial wave functions $\Phi_{L(R)}(\mathbf{r})$ mostly localized on the left (right) side of the trap:

$$\Psi(\mathbf{r};t) = \Psi_L(t)\Phi_L(\mathbf{r}) + \Psi_R(t)\Phi_R(\mathbf{r}). \tag{3}$$

The left and right modes can be expressed as linear combinations of the ground state (+) and the first solitonic eigenstate (−) of the double-well potential including the interaction term. They satisfy $(H_0 + H_g[\Phi_\pm])\Phi_\pm = \mu_\pm \Phi_\pm$, and the left/right modes can be written as [14]

$$\Phi_L(\mathbf{r}) = \frac{\Phi_+(\mathbf{r}) + \Phi_-(\mathbf{r})}{\sqrt{2}}, \quad \Phi_R(\mathbf{r}) = \frac{\Phi_+(\mathbf{r}) - \Phi_-(\mathbf{r})}{\sqrt{2}}. \tag{4}$$

We observe that in a symmetric double well, $\Phi_\pm$ have a well-defined parity: $\Phi_\pm(\mathbf{r}) = \pm\Phi_\pm(-\mathbf{r})$, and therefore $\langle \Phi_i \Phi_j \rangle = \delta_{ij}$ with $i, j = +, -$. Since they are stationary solutions of the GP equation, $\Phi_\pm$ are real functions, and so are the left and right modes $\Phi_{L(R)}$. The integrated density in the z-direction, $\rho(x, y) = \int dz |\Psi(x, y, z)|^2$, associated with the ground (Φ_+) and first excited (Φ_-) states is depicted in figure 1 together with the densities associated with the left and right modes. The plots correspond to the experimental setup of [4].

From the phase coherence properties of a BEC, one can assume that the wave function on each side of the trap has a well-defined quantum phase $\phi_j(t)$, which is independent of the position but changes during the time evolution. We can write

$$\Psi_j(t) = \sqrt{N_j(t)}\, e^{i\phi_j(t)}, \tag{5}$$

where $N_{L(R)}(t)$ corresponds to the number of atoms on the left (right) side of the trap, and the total number of atoms is $N = N_L(t) + N_R(t)$. The weak link condition is fulfilled if $(\mu_- - \mu_+) \ll (1/2)(\mu_+ + \mu_-)$.

---

[7] Note that this is zero if the barrier is infinitely high.
[8] Note that we explicitly stay within the GP applicability; for instance, if the barrier height were too high, the two condensates would fragment.
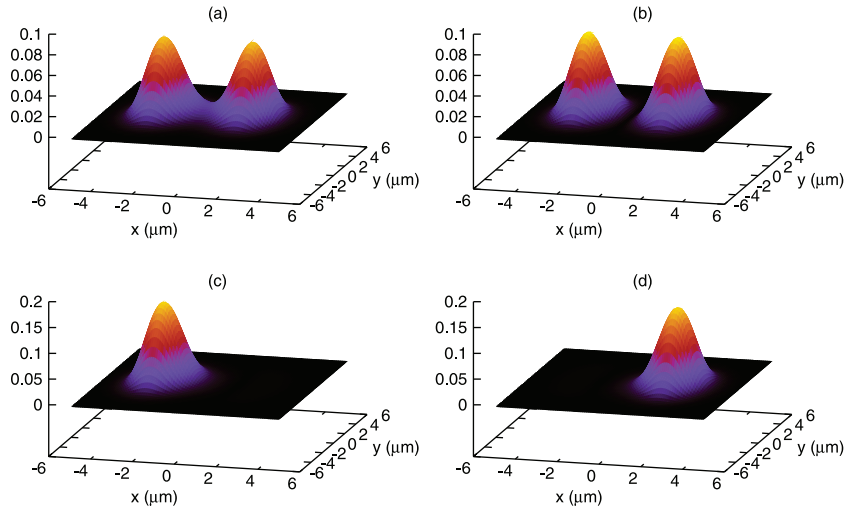
Figure 1. 3D depictions of the density, $\rho(x, y) = \int dz |\Psi(x, y, z)|^2$ in $(\mu m)^{-2}$, of (a) the ground state, (b) the first excited state, (c) the left mode and (d) the right mode obtained by performing an imaginary time GP3D calculation with the same conditions as in the experimental setup of [4].

As a first step, we consider the so-called standard two-mode approximation (S2M), which neglects a certain set of overlapping integrals involving mixed products of Φ_L and Φ_R. This approximation yields essentially the correct qualitative results in the scalar condensate when compared with the GP equation although it may lead to different quantitative predictions depending on the specific barrier properties [4, 14].

Inserting the two-mode ansatz (3) into the GP equation for a single component condensate (2) and neglecting terms involving mixed products of Φ_L and Φ_R of order larger than 1 yields a system of equations for the two localized modes that can be written in terms of two dynamical variables: the population imbalance $z(t) = [N_L(t) - N_R(t)]/N$ and the phase difference $\delta\phi(t) = \phi_R(t) - \phi_L(t)$ between each side of the barrier [7, 9, 10]

$$\dot{z}(t) = -\omega_R \sqrt{1 - z^2(t)} \, \sin\delta\phi(t),$$

$$\dot{\delta\phi}(t) = \omega_R \, \Delta E + \omega_R \frac{U_L + U_R}{4\,K} N z(t) + \omega_R \frac{z(t)}{\sqrt{1 - z^2(t)}} \, \cos\delta\phi(t), \tag{6}$$

where $\omega_R = 2K/\hbar$ is the Rabi frequency and

$$\Delta E = \frac{E_L^0 - E_R^0}{2K} + \frac{U_L - U_R}{4K} N,$$

$$E_{L(R)}^0 = \int d\mathbf{r} \left[\frac{\hbar^2}{2m} |\nabla \Phi_{L(R)}(\mathbf{r})|^2 + \Phi_{L(R)}^2(\mathbf{r}) \, V(\mathbf{r}) \right],$$

$$K = -\int d\mathbf{r} \left[\frac{\hbar^2}{2m} \nabla \Phi_L(\mathbf{r}) \cdot \nabla \Phi_R(\mathbf{r}) + \Phi_L(\mathbf{r}) \, V(\mathbf{r}) \, \Phi_R(\mathbf{r}) \right], \tag{7}$$

$$U_{L(R)} = g \int d\mathbf{r} \, \Phi_{L(R)}^4(\mathbf{r}).$$

For a symmetric double well, $E_L^0 = E_R^0$ and $U_L = U_R \equiv U$; therefore $\Delta E = 0$. Moreover, the Rabi frequency only appears as a scale in the problem and thus can be absorbed in the time by rescaling $t \to \omega_R t$. Then, together with the definition $\Lambda \equiv NU/(\hbar \omega_R)$, we obtain

$$\dot{z}(t) = -\sqrt{1 - z^2(t)} \, \sin \delta\phi(t),$$

$$\dot{\delta\phi}(t) = \Lambda z(t) + \frac{z(t)}{\sqrt{1 - z^2(t)}} \cos \delta\phi(t). \tag{8}$$

Note that $\Lambda > 0$ and $\Lambda < 0$ correspond to repulsive and attractive atom–atom interactions, respectively. There are different regimes depending on the initial values of the population imbalance and phase difference, $z(0)$ and $\delta\phi(0)$; see section 3.3.

From the energy functional of the GP equation (2),

$$E[\Psi(\mathbf{r}; t)] = \int d\mathbf{r} \left[\frac{\hbar^2}{2m} |\vec{\nabla} \Psi(\mathbf{r}; t)|^2 + V(\mathbf{r}) |\Psi(\mathbf{r}; t)|^2 + \frac{g}{2} |\Psi(\mathbf{r}; t)|^4 \right], \tag{9}$$

and using the two-mode ansatz (3), we can define the conserved energy per particle of the system as

$$H \equiv \frac{E[\Psi(\mathbf{r}; t)] - C}{NK} = \Delta E \, z(t) + \frac{U_L + U_R}{8K} N z^2(t) - \sqrt{1 - z^2(t)} \cos \delta\phi(t), \tag{10}$$

where C is a rescaling constant. If we consider again a symmetric double well, we have

$$H = \frac{\Lambda}{2} z^2(t) - \sqrt{1 - z^2(t)} \cos \delta\phi(t). \tag{11}$$

Note that the equations of motion (8) can be written in the Hamiltonian form

$$\dot{z} = -\frac{\partial H}{\partial \delta\phi}, \quad \dot{\delta\phi} = \frac{\partial H}{\partial z}, \tag{12}$$

with z and $\delta\phi$ being canonical conjugate variables.

3.2. Improved two-mode model for the single component case

Smerzi and collaborators [11, 12] noted that for a symmetric double well there was no need to neglect any of the overlapping integrals to obtain a closed set of equations relating z and $\delta\phi$. Thus, remaining in the two-mode approximation but retaining all the overlaps it is straightforward to write down the following set of equations (cf equations (22) of [14]), called the 'improved two-mode' (I2M) equations,

$$\dot{z}(t) = -B\sqrt{1 - z^2(t)} \, \sin \delta\phi(t) + C(1 - z^2(t)) \sin 2\delta\phi(t),$$

$$\dot{\delta\phi}(t) = A z(t) + \frac{B z(t)}{\sqrt{1 - z^2(t)}} \cos \delta\phi(t) - C z(t) \cos 2\delta\phi(t). \tag{13}$$

Defining $\gamma_{ij} = g \int d\mathbf{r} \, \Phi_i^2(\mathbf{r}) \Phi_j^2(\mathbf{r})$, $i, j = +, -$, we have $A = N(10\gamma_{+-} - \gamma_{++} - \gamma_{-})/4$, $B = 2K + N(\gamma_- - \gamma_{++})/2$, and $C = gN \int d\mathbf{r} \, \Phi_L^2(\mathbf{r}) \Phi_R^2(\mathbf{r})$.

As discussed in detail in [14], the physics arising from the I2M is similar to that present in the S2M if C is sufficiently small. This is the case for the potential considered in [4]. The overlaps included in B (and not the ones incorporated into C) when using the improved

Table 1. Stationary points of the system for repulsive interactions, $\Lambda > 0$, and their stability.

$(z^0, \delta\phi^0)$	Stationary	Minimum	Saddle	Maximum
$(0, 0)$	$\forall\Lambda$	$\forall\Lambda$	—	—
$(0, \pi)$	$\forall\Lambda$	—	$\Lambda > 1$	$\Lambda < 1$
$(\pm\sqrt{1 - 1/\Lambda^2}, \pi)$	$\Lambda > 1$	—	—	$\Lambda > 1$
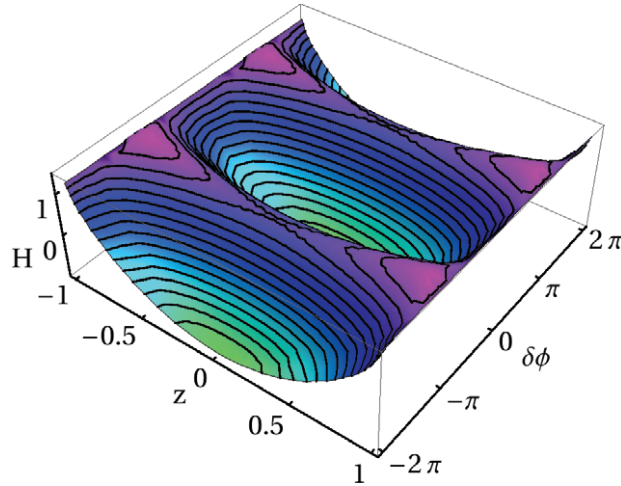
Figure 2. Energy surface, equation (11), for $\Lambda = 2.5$. The lines on the surface correspond to possible trajectories of the system.

two-mode approach are responsible for much better quantitative agreement with the GP3D, as we will see in section 5.

3.3. Regimes for the single component case

3.3.1. Stability analysis. In this section we use the S2M to analyze the stability of the single component system and focus on the case of repulsive interactions $\Lambda > 0$. Using the Hamiltonian (11) and the equations of motion (12), the stationary points $(z^0, \delta\phi^0)$ can be found by solving the equations

$$\frac{\partial H}{\partial z}\bigg|_{z^0, \delta\phi^0} = 0, \qquad \frac{\partial H}{\partial \delta\phi}\bigg|_{z^0, \delta\phi^0} = 0. \qquad (14)$$

To assess the stability of these points, we need to study the Hessian matrix of the system, which for the possible values of the phase difference, $\delta\phi^0 = 0$ or π, is always diagonal and its eigenvalues are $\partial_z^2 H|_{z^0, \delta\phi^0}$ and $\partial_{\delta\phi}^2 H|_{z^0, \delta\phi^0}$. Depending on the sign of these eigenvalues the stationary points will be maxima, saddle points or minima. The stationary points and their stability are summarized in table 1.

The evolution of the system can be represented on a z–$\delta\phi$ plane, where the system follows trajectories with constant energy, H; see curves in figure 2. Note that oscillations around a stationary point, closed curves, occur only if the central point is either a maximum or a minimum
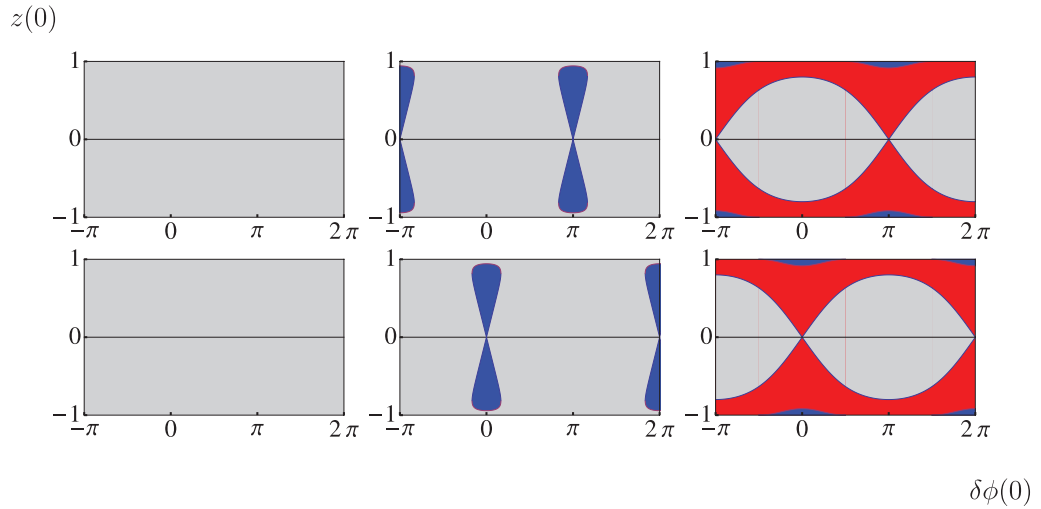
Figure 3. Different regimes for a set of initial conditions, imbalance $z(0)$ in the y-axis and phase difference $\delta\phi(0)$ in the x-axis. The upper panels correspond to repulsive interactions and the lower ones to attractive interactions. The values of $|\Lambda|$ are 0.5, 1.5 and 5 for the left, middle and right panels respectively. Grey regions correspond to Josephson oscillations, blue regions to π-modes (upper panels) and zero-modes (lower panels), and red regions to running phase modes.

of the energy, but not a saddle point. As we will see in the following sections, these orbits will give rise to the Josephson oscillations and to the zero- and π-modes [9].

3.3.2. Symmetry between attractive and repulsive interactions. The stability analysis has been presented only for repulsive interactions, but from the system (8) we can see that if we change the interactions, $\Lambda \longrightarrow -\Lambda$, we recover the same system of equations if $\delta\phi \longrightarrow \pi - \delta\phi$:

$$
\begin{aligned}
\frac{\mathrm{d}}{\mathrm{d}t}z(t) &= -\sqrt{1 - z^2(t)}\,\sin(\pi - \delta\phi(t)), \\
\frac{\mathrm{d}}{\mathrm{d}t}(\pi - \delta\phi(t)) &= -\Lambda z(t) - \frac{z(t)}{\sqrt{1 - z^2(t)}}\,\cos(\pi - \delta\phi(t)),
\end{aligned}
\tag{15}
$$

which means that the dynamics of the system and the different regimes are the same for both interactions, with a phase shift of π. This can be seen in figure 3, which shows the behavior of the system for a given set of initial conditions. The upper panels are for repulsive interactions $\Lambda > 0$ and the lower ones for attractive interactions $\Lambda < 0$. The grey regions correspond to Josephson oscillations, the blue regions to zero- and π-modes and the red regions to running phase modes, as will be seen in the following sections.

3.3.3. Josephson dynamics. This regime is characterized by fast oscillating tunneling of population across the potential barrier. Plotted in a z–$\delta\phi$ map, the system evolves following closed trajectories around a minimum or a maximum ($z^0 = 0$, $\delta\phi^0$) configuration, with a zero time average of the population imbalance, $\langle z \rangle_t = 0$. The stability analysis shows that for $\Lambda > -1$, which corresponds to repulsive or slightly attractive interactions, the stationary point
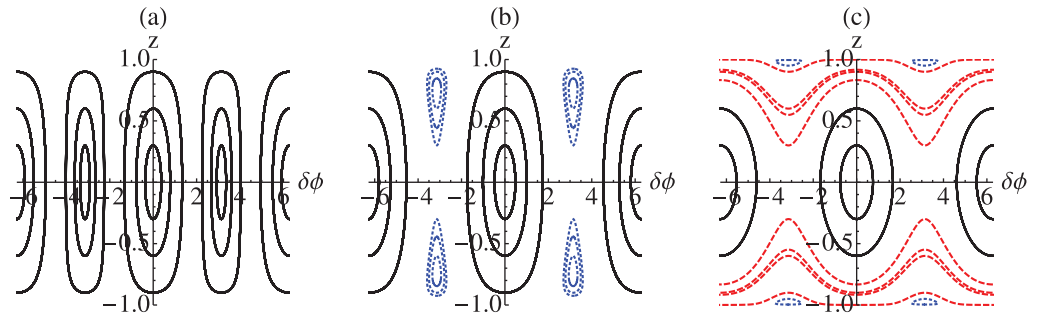
Figure 4. z–$\delta\phi$ representation of different constant energy trajectories for three values of Λ: 0.5 (a), 1.5 (b) and 5 (c). Solid black lines correspond to Josephson oscillations, dotted blue lines to π-modes and dashed red lines to running phase modes.

$(z^0 = 0, \delta\phi^0 = 0)$ is a minimum permitting Josephson oscillations around it. Analogously, for $\Lambda < 1$, either attractive or slightly repulsive interactions, the stationary point $(z^0 = 0, \delta\phi^0 = \pi)$ becomes a maximum, and therefore also allows for closed orbits around it. For $|\Lambda| > 1$, there are Josephson oscillations around only one point: $(z^0 = 0, \delta\phi^0 = 0)$ or $(z^0 = 0, \delta\phi^0 = \pi)$. However, in the region of weak interaction, $|\Lambda| < 1$, the oscillations around both points are allowed.

In panel (a) of figure 4, $\Lambda = 0.5$, the black closed orbits around $\delta\phi^0 = 0$ or around $\delta\phi^0 = \pi$ correspond to Josephson dynamics around these points. In panel (b) however, as $\Lambda = 1.5 > 1$, only the origin can give rise to Josephson oscillations, so the closed orbits around $(z^0 = 0, \delta\phi^0 = \pi)$ disappear.

It is also interesting to study the behavior of the system for small oscillations around these two stationary points of zero imbalance, smallest orbits in figure 4(a). In this limit, the system (8) can be linearized giving the dynamical equation: $\ddot{z}(t) = -z(t)(1 + \Lambda \cos \delta\phi^0)$ with $\cos \delta\phi^0 = \pm 1$. The population imbalance performs sinusoidal oscillations with a frequency $\omega_J = \omega_R \sqrt{1 + \Lambda \cos \delta\phi^0}$, independent of the initial conditions. Note that this frequency only exists when these points are either maxima or minima. The phase difference oscillates with the same frequency but with a phase shift of $\pi/2$ with respect to the imbalance. If the initial population imbalance increases, the dynamics of the system changes substantially to non-sinusoidal oscillations, and the frequency becomes dependent on the initial conditions.

3.3.4. Macroscopic quantum self-trapping (MQST). In the case of repulsive interactions, we have seen that for $\Lambda > 1$, the stationary point $(z^0 = 0, \delta\phi^0 = \pi)$ becomes a saddle point and there appear two maxima, $(z^0 = \pm\sqrt{1 - 1/\Lambda^2}, \delta\phi^0 = \pi)$. Similar behavior is found for attractive interactions. These stationary points allow for oscillations around them with $\langle z \rangle_t \neq 0$. In fact, in this regime, the imbalance has the same sign during the evolution, and therefore one of the wells is always overpopulated.

This regime is called macroscopic quantum self trapping as the tunneling is strongly suppressed and the particles remain mostly trapped in one of the wells. This is a phenomenon arising from the atom–atom interaction, which appears as a nonlinearity in the Gross–Pitaevskii equation.

The critical condition for the existence of the MQST regime can be found by imposing that the system remains on one side of the trap [7]. For a given set of initial conditions, $z(0) \neq 0$ and

IOP Institute of Physics **Φ** DEUTSCHE PHYSIKALISCHE GESELLSCHAFT

$\delta\phi(0)$, the system will remain trapped if

$$\Lambda > 2\left(\frac{\sqrt{1-z(0)^2}\cos[\delta\phi(0)]+1}{z(0)^2}\right) \quad \text{for } \Lambda > 1,$$

$$\Lambda < 2\left(\frac{\sqrt{1-z(0)^2}\cos[\delta\phi(0)]-1}{z(0)^2}\right) \quad \text{for } \Lambda < -1, \tag{16}$$

where the limits of the interaction parameter are due to the fact that only when $|\Lambda| > 1$ do the $(z^0 \neq 0, \delta\phi^0)$ stationary points exist.

In this regime however, there are two different kinds of MQST depending on whether the phase difference evolves bounded, giving the so-called zero- and π-modes [9], or whether it evolves unbounded, increasing (or decreasing) always in time, giving rise to the running phase modes.

For values of the interaction parameter of $1 < |\Lambda| < 2$ the only MQST regime that one can have is the zero mode for attractive interactions and the π-mode for repulsive interactions (which are plotted in blue dotted lines in panel (b) of figure 4). In these regimes the phase difference evolves bounded around $\delta\phi = 0$ and $\delta\phi = \pi$, respectively.

On the other hand, for values of $|\Lambda| > 2$ one can have both classes of MQST. In general however, for a given set of initial conditions, the system will evolve following a running phase mode (dashed red lines of panel (c) of figure 4), because the values of $z^0 = \pm\sqrt{1 - 1/\Lambda^2}$, which allow closed orbits, are very close to 1 (see the small π-modes of panel (c) in blue dotted lines).

In panel (c), one can infer that the broadest closed orbit around $(z^0 \neq 0, \delta\phi^0 = \pi)$, for $\Lambda > 2$, is the one that goes through $(z = \pm 1, \delta\phi = 0)$. Note that an orbit that crosses the $\delta\phi = 0$ axis at any other point, $z \neq \pm 1$, would correspond to a running phase mode. The case of attractive interactions can be understood by taking into account the phase shift of π in $\delta\phi$. The latter can be used to find the condition to have bounded or running phase difference modes. For a given set of initial conditions $(z(0), \delta\phi(0))$ fulfilling the self-trapping condition (16), the system will evolve in a bounded phase mode only if

$$|\Lambda| < \frac{2\cos\delta\phi(0)}{\sqrt{1-z^2(0)}}. \tag{17}$$

Moreover, in a zero- or a π-mode MQST, we can study small oscillations around the corresponding minima or maxima, $z(t) = z^0 + \delta z$ and $\delta\phi(t) = \delta\phi^0 + \hat{\delta\phi}(t)$, so the linearized system (8) becomes

$$\delta\ddot{z}(t) = -\delta z(t)\left[1 + \Lambda\cos\delta\phi^0\frac{1-2(z^0)^2}{\sqrt{1-(z^0)^2}}\right], \tag{18}$$

which gives sinusoidal behavior with a frequency

$$\omega = \omega_R\sqrt{1 + \Lambda\cos\delta\phi^0\frac{1-2(z^0)^2}{\sqrt{1-(z^0)^2}}}. \tag{19}$$

3.4. Standard two-mode model for the binary mixture

Let us recall the two-mode approximation for weakly linked binary mixtures [27]–[30]. The total wave function of each component is written as a superposition of two time-independent

spatial wave functions localized in each well:

$$\Psi_j(\mathbf{r}; t) = \Psi_{jL}(t)\Phi_{jL}(\mathbf{r}) + \Psi_{jR}(t)\Phi_{jR}(\mathbf{r}), \tag{20}$$

with $\langle\Phi_{i\alpha}|\Phi_{j\beta}\rangle = \delta_{ij}\delta_{\alpha\beta}$, $i,j = a, b$ and $\alpha, \beta = L, R$. For a given component, the condensates on each side of the trap are weakly linked. Then, as in the scalar case, one can assume that the wave function in each side of the trap has a well-defined quantum phase $\phi_{j,\alpha}(t)$, which is independent of the position but which changes during the time evolution. Thus,

$$\Psi_{j,\alpha}(t) = \sqrt{N_{j,\alpha}(t)}e^{i\phi_{j,\alpha}(t)}. \tag{21}$$

$N_{j,L(R)}(t)$ corresponds to the population of the j-component on the left (right) side of the trap, with $N_j = N_{j,L}(t) + N_{j,R}(t)$. Inserting the two-mode ansatz (20) in the coupled GP equations for the mixture (1), retaining up to first order crossed terms yields the following system of coupled equations [7]:

$$\dot{z_a}(t) = -\frac{2K_a}{\hbar}\sqrt{1 - z_a^2(t)}\sin\delta\phi_a(t),$$

$$\delta\dot{\phi}_a(t) = \Delta E_{a,b} + \frac{U_{aaL} + U_{aaR}}{2\hbar}N_a z_a(t) + \frac{U_{abL} + U_{abR}}{2\hbar}N_b z_b(t) + \frac{2K_a}{\hbar}\frac{z_a(t)}{\sqrt{1 - z_a^2(t)}}\cos\delta\phi_a(t),$$

$$\dot{z_b}(t) = -\frac{2K_b}{\hbar}\sqrt{1 - z_b^2(t)}\sin\delta\phi_b(t), \tag{22}$$

$$\delta\dot{\phi}_b(t) = \Delta E_{b,a} + \frac{U_{bbL} + U_{bbR}}{2\hbar}N_b z_b(t) + \frac{U_{baL} + U_{baR}}{2\hbar}N_a z_a(t)\frac{2K_b}{\hbar}\frac{z_b(t)}{\sqrt{1 - z_b^2(t)}}\cos\delta\phi_b(t),$$

where

$$\Delta E_{i,j} = \frac{E_{iL}^0 - E_{iR}^0}{\hbar} + \frac{U_{iiL} - U_{iiR}}{2\hbar}N_i + \frac{U_{ijL} - U_{ijR}}{2\hbar}N_j,$$

$$E_{j\alpha}^0 = \int d\mathbf{r}\left[\frac{\hbar^2}{2m_j}|\nabla\Phi_{j\alpha}(\mathbf{r})|^2 + \Phi_{j\alpha}^2 V(\mathbf{r})\right],$$

$$K_j = -\int d\mathbf{r}\left[\frac{\hbar^2}{2m_j}\nabla\Phi_{jL}(\mathbf{r})\cdot\nabla\Phi_{jR}(\mathbf{r}) + \Phi_{jL}(\mathbf{r}) V(\mathbf{r})\Phi_{jR}(\mathbf{r})\right], \tag{23}$$

$$U_{ij\alpha} = g_{ij}\int d\mathbf{r}\,\Phi_{i\alpha}^2(\mathbf{r})\Phi_{j\alpha}^2(\mathbf{r}),$$

with $i, j = a, b$ and $\alpha = L, R$. Let us consider a mixture with the same atomic mass for both components $M \equiv m_a = m_b$, which are trapped in the same symmetric double-well potential. Then, the localized modes are the same for both components but depend on the site $\Phi_{L(R)} \equiv \Phi_{a,L(R)} = \Phi_{b,L(R)}$. Therefore, $E_{aL}^0 = E_{bL}^0 = E_{aR}^0 = E_{bR}^0 \equiv E$, $U_{aaL} = U_{bbL} = U_{aaR} = U_{bbR} \equiv U$ and $U_{abL} = U_{baL} = U_{abR} = U_{baR} \equiv \tilde{U}$, $K_a = K_b \equiv K$. Defining for each component the population imbalance and phase difference between both sides of the barrier,

$$z_j(t) = (N_{j,L}(t) - N_{j,R}(t))/N_j, \quad \delta\phi_j(t) = \phi_{j,R}(t) - \phi_{j,L}(t), \tag{24}$$

the above equations can be rewritten as

$$\dot{z_a}(t) = -\omega_R \sqrt{1 - z_a^2(t)} \, \sin \delta\phi_a(t),$$

$$\delta\dot{\phi}_a(t) = \frac{N_a U z_a(t) + N_b \tilde{U} z_b(t)}{\hbar} + \omega_R \frac{z_a(t)}{\sqrt{1 - z_a^2(t)}} \, \cos \delta\phi_a(t),$$

$$\dot{z_b}(t) = -\omega_R \sqrt{1 - z_b^2(t)} \, \sin \delta\phi_b(t), \tag{25}$$

$$\delta\dot{\phi}_b(t) = \frac{N_b U z_b(t) + N_a \tilde{U} z_a(t)}{\hbar} + \omega_R \frac{z_b(t)}{\sqrt{1 - z_b^2(t)}} \, \cos \delta\phi_b(t),$$

where $\omega_R = 2K/\hbar$ is the Rabi frequency, the same for both species. It is useful to define $\Lambda = NU/\hbar\omega_R$, $\tilde{\Lambda} = N\tilde{U}/\hbar\omega_R$, $f_a = N_a/N$, $f_b = N_b/N$ and rescale the time as $t \to \omega_R t$,

$$\dot{z_a}(t) = -\sqrt{1 - z_a^2(t)} \, \sin \delta\phi_a(t),$$

$$\delta\dot{\phi}_a(t) = f_a \Lambda z_a(t) + f_b \tilde{\Lambda} z_b(t) + \frac{z_a(t)}{\sqrt{1 - z_a^2(t)}} \, \cos \delta\phi_a(t),$$

$$\dot{z_b}(t) = -\sqrt{1 - z_b^2(t)} \, \sin \delta\phi_b(t), \tag{26}$$

$$\delta\dot{\phi}_b(t) = f_b \Lambda z_b(t) + f_a \tilde{\Lambda} z_a(t) + \frac{z_b(t)}{\sqrt{1 - z_b^2(t)}} \, \cos \delta\phi_b(t).$$

These equations correspond to two coupled non-rigid pendulums. The stability of these systems of equations has been analyzed recently in [29].

3.5. Improved two-mode model for the binary mixture

As was noted for the scalar case in [11], it is not mandatory to neglect any of the overlaps to obtain a closed set of equations relating the population imbalances and phase differences for a symmetric double-well potential. The complete set of two-mode equations was called the improved two-mode (I2M) equations.

In principle, if the experimental setup is appropriately chosen such that the mean-field conditions are valid, the GP equation is expected to show quantitative agreement with the experimental results. Moreover, if the left and right modes are well localized on each side of the trap, the S2M equations are expected to provide a good description of the GP equation. When the two modes are not so well localized, it becomes necessary to consider the I2M to have quantitative agreement with the GP results. In [14], the authors considered explicitly the setup of the Heidelberg group and showed that the I2M is necessary in the single component case in order to provide a quantitative understanding of the experimental data.

Following similar steps as in the previous section and assuming the double-well potential to be symmetric as in the experiment, the wave functions for the ground state and first excited state, $\Phi_{j\pm}(\mathbf{r})$, have a well-defined parity. The symmetry properties and the orthonormalization conditions are capital to derive the coupled equations within the I2M model: $\Phi_{j\pm}(\mathbf{r}) = \pm\Phi_{j\pm}(-\mathbf{r})$, $\langle\Phi_{i\alpha}|\Phi_{j\beta}\rangle = \delta_{ij}\delta_{\alpha\beta}$, for $i, j = a, b$ and $\alpha, \beta = +, -$. The I2M provides an exact

description of the dynamics in the symmetric double-well potential, with no approximations beyond the assumption of a two-mode ansatz of the total wave function $\Psi_j(\mathbf{r}; t)$, equation (20).

The resulting system of equations relating the population imbalance and phase difference for each component within the I2M approximation reads[9]

$$\dot{z}_a(t) = -\frac{2K_{ab}}{\hbar}\sqrt{1 - z_a^2(t)}\sin\delta\phi_a(t),$$

$$\dot{\delta\phi}_a(t) = \frac{\Delta_a(t)}{\hbar} + \frac{2K_{ab}(t)}{\hbar}\frac{z_a(t)}{\sqrt{1 - z_a^2(t)}}\cos\delta\phi_a(t),$$

$$\dot{z}_b(t) = -\frac{2K_{ba}(t)}{\hbar}\sqrt{1 - z_b^2(t)}\sin\delta\phi_b(t),$$

$$\dot{\delta\phi}_b(t) = \frac{\Delta_b(t)}{\hbar} + \frac{2K_{ba}(t)}{\hbar}\frac{z_b(t)}{\sqrt{1 - z_b^2(t)}}\cos\delta\phi_b(t)$$

(27)

with

$$\Delta_a(t) = 2\,\gamma_{+-}^{aa}N_a\,z_a(t) + 2\,\gamma_{+-+-}^{aabb}\,N_b z_b(t),$$

$$\Delta_b(t) = 2\,\gamma_{+-}^{bb}N_b z_b(t) + 2\,\gamma_{+-+-}^{bbaa}\,N_a z_a(t),$$

(28)

where we have defined

$$\gamma_{\alpha\beta}^{ij} = g_{ij}\int d\mathbf{r}\,\Phi_{i\alpha}^2(\mathbf{r})\Phi_{j\beta}^2(\mathbf{r}),$$

$$\gamma_{+-+-}^{aabb} = \gamma_{+-+-}^{bbaa} = g_{ab}\int d\mathbf{r}\,\Phi_{a+}(\mathbf{r})\Phi_{a-}(\mathbf{r})\Phi_{b+}(\mathbf{r})\Phi_{b-}(\mathbf{r}),$$

(29)

and

$$2K_{ab}(t) = (\mu_-^a - \mu_+^a) + \frac{1}{2}\Big[N_a\left(\gamma_{++}^{aa} - \gamma_{--}^{aa}\right) + N_b\left(\gamma_{++}^{ab} - \gamma_{--}^{ab} - \gamma_{+-}^{ab} + \gamma_{-+}^{ab}\right)$$

$$- N_a\left(\gamma_{++}^{aa} + \gamma_{--}^{aa} - 2\gamma_{+-}^{aa}\right)\sqrt{1 - z_a^2(t)}\cos\delta\phi_a(t)$$

$$- N_b\left(\gamma_{++}^{ab} + \gamma_{--}^{ab} - \gamma_{+-}^{ab} - \gamma_{-+}^{ab}\right)\sqrt{1 - z_b^2(t)}\cos\delta\phi_b(t)\Big].$$

(30)

μ_+^j and μ_-^j are the chemical potentials of the ground and first excited states of the j component, which can be calculated from the time-independent GP equation for $\Phi_{j\pm}$, respectively. Analogously, one can define $2K_{ba}$ by exchanging the subscripts a and b in the previous expression.

Note that we have kept the full 3D dependence of the wave functions $\Phi_{j\pm}(\mathbf{r})$, instead of averaging the transverse spatial dependence as in [14, 30]. Thus, the coupling parameters g_{ij} in equations (29) are the 3D ones and are not renormalized.

The equations for the I2M are essentially similar to the S2M. The main difference is that the tunneling term, $K_{ab}(t)$, is time dependent and contains effects due to the interactions. As expected, if the localization of the modes is increased, i.e. by increasing the barrier height, $K_{ab}(t)$ approaches the constant value, $2K_{ab} \to \mu_-^a - \mu_+^a$, which equals $2K$ of equation (23). The coupled equations obtained in the I2M model reduce to well-known dynamical equations

[9] Our system of equations differs slightly from the previously derived ones, cf the appendix of [30]. We believe that their system has some minor errors, which do not affect their discussion, which is based on the S2M equations.

in two limiting cases:

(i) Setting to zero the overlapping integrals that involve mixed products of left and right modes of order larger than 1, the I2M equations reduce to the S2M model for the mixture, equations (25).

(ii) Assuming a non-interacting mixture, the inter-species interaction is $g_{ab} = 0$, and the I2M equations for the mixture reduce to two non-coupled system of equations, which are the dynamical equations of the I2M for a single component, section 3.2.

As discussed in the introduction, we are interested in the particular case of a binary mixture made of atoms populating two different hyperfine states. Then, both components have the same mass M, and are trapped in the same symmetric double-well potential. We initially restrict ourselves to the case in which the inter-species interaction is also almost equal to the intra-species one, $g \equiv g_{aa} = g_{bb} \sim g_{ab}$. This is the situation for $F = 1$, $m = \pm 1$ of ^{87}Rb. This case allows straightforward comparisons between the results of the I2M and the ones obtained by solving the NPSE or GP1D for a mixture explained in section 4.

The ground and first excited states in a symmetric double-well potential are the same for both components. Moreover, since $g = g_{ab}$ the overlap integrals (29) reduce to

$$\gamma^{aa}_{++} = \gamma^{bb}_{++} = \gamma^{ab}_{++} \equiv \gamma_{++},$$

$$\gamma^{aa}_{--} = \gamma^{bb}_{--} = \gamma^{ab}_{--} \equiv \gamma_{--}, \tag{31}$$

$$\gamma^{aa}_{+-} = \gamma^{bb}_{+-} = \gamma^{ab}_{+-} = \gamma^{ab}_{-+} = \gamma^{aabb}_{+-+-} \equiv \gamma_{+-},$$

and the chemical potentials $\mu^a_\alpha = \mu^b_\alpha \equiv \mu_\alpha$ with $\alpha = +, -$. This yields the following relations: $K_{ab} = K_{ba}$ and $\Delta_a = \Delta_b$. The I2M system reduces to

$$\dot{z}_a(t) = -\frac{2K_{ab}(t)}{\hbar}\sqrt{1 - z_a^2(t)}\sin\delta\phi_a(t),$$

$$\dot{\delta\phi}_a(t) = \frac{2(N_a z_a(t) + N_b z_b(t))\gamma_{+-}}{\hbar} + \frac{2K_{ab}(t)}{\hbar}\frac{z_a(t)}{\sqrt{1 - z_a^2(t)}}\cos\delta\phi_a(t),$$

$$\dot{z}_b(t) = -\frac{2K_{ab}(t)}{\hbar}\sqrt{1 - z_b^2(t)}\sin\delta\phi_b, \tag{32}$$

$$\dot{\delta\phi}_b(t) = \frac{2(N_a z_a(t) + N_b z_b(t))\gamma_{+-}}{\hbar} + \frac{2K_{ab}(t)}{\hbar}\frac{z_b(t)}{\sqrt{1 - z_b^2(t)}}\cos\delta\phi_b(t).$$

In this case both components obey the same system of coupled differential equations. Then, if the initial conditions are the same for both $z_a(0) = z_b(0)$ and $\delta\phi_a(0) = \delta\phi_b(0)$, they will evolve with the same imbalance and phase, and no mixture effects will be observed.

3.6. Regimes for binary mixtures

We proceed now to analyze the stability of the system of equations (26), cf the appendix of [27]. As in the single component case, and in order to get analytical results that allow for a physical

insight, we perform the study in the framework of the S2M approximation. First we note that a stationary point, defined by the equations $\dot{z}_i = 0$ and $\dot{\delta\phi_i} = 0$, necessarily fulfills

$$\sin\delta\phi_a = 0, \Rightarrow \delta\phi_a^0 = 0, \pi,$$
$$\sin\delta\phi_b = 0, \Rightarrow \delta\phi_b^0 = 0, \pi,$$

(33)

and the following system of equations:

$$z_a^0 = -z_b^0 \left(\frac{\Lambda}{\tilde{\Lambda}} + \frac{1}{\tilde{\Lambda} f_b \sqrt{1 - (z_b^0)^2} \cos\delta\phi_b^0} \right),$$

$$z_b^0 = -z_a^0 \left(\frac{\Lambda}{\tilde{\Lambda}} + \frac{1}{\tilde{\Lambda} f_a \sqrt{1 - (z_a^0)^2} \cos\delta\phi_a^0} \right).$$

(34)

Therefore there are four different cases: $(\delta\phi_a^0 = 0, \delta\phi_b^0 = 0)$, $(\delta\phi_a^0 = 0, \delta\phi_b^0 = \pi)$, $(\delta\phi_a^0 = \pi, \delta\phi_b^0 = 0)$, $(\delta\phi_a^0 = \pi, \delta\phi_b^0 = \pi)$, noting that in all of them there is an obvious stationary point, $z_a^0 = z_b^0 = 0$. These stationary points will be referred to as 'trivial stationary points'. We need to find the conditions for non-trivial solutions in each case.

The stability of the system is analyzed by considering small variations around the stationary points for each of the four situations. Defining the displacements η_i,

$$z_a(t) = z_a^0 + \eta_a(t),$$
$$z_b(t) = z_b^0 + \eta_b(t),$$

(35)

the following system of equations for the η's can be derived from equations (26)

$$\begin{pmatrix} \ddot{\eta}_a \\ \ddot{\eta}_b \end{pmatrix} = -\Omega^2 \begin{pmatrix} \eta_a \\ \eta_b \end{pmatrix},$$

(36)

where

$$\Omega^2 = \omega_R^2 \begin{pmatrix} 1 + (f_a \Lambda z_a^0 + f_b \tilde{\Lambda} z_b^0)^2 & 0 \\ 0 & 1 + (f_a \tilde{\Lambda} z_a^0 + f_b \Lambda z_b^0)^2 \end{pmatrix}$$

$$+ \omega_R^2 \begin{pmatrix} f_a \Lambda \sqrt{1 - (z_a^0)^2} \cos\delta\phi_a^0 & f_a \tilde{\Lambda} \sqrt{1 - (z_a^0)^2} \cos\delta\phi_a^0 \\ f_b \tilde{\Lambda} \sqrt{1 - (z_b^0)^2} \cos\delta\phi_b^0 & f_b \Lambda \sqrt{1 - (z_b^0)^2} \cos\delta\phi_b^0 \end{pmatrix}.$$

(37)

In table 2 we give the explicit values of the eigenfrequencies of Ω for the trivial stationary points, $z_i^0 = 0$. These are obtained for $\Lambda > 0$ and $\tilde{\Lambda} > 0$. Approximate simpler expressions for these eigenfrequencies can be derived when $\tilde{\Lambda} \sim \Lambda$. Defining $\tilde{\Lambda} = \Lambda(1 + \beta)$ and retaining up to terms of order β, one obtains the frequencies listed in table 3.

3.6.1. Stationary points with $(\delta\phi_a^0 = 0, \delta\phi_b^0 = 0)$. In this case, the condition for the existence of non-trivial solutions to equations (34) depends on the slope at the origin of the two curves (34) [27]. The condition

$$\left(\frac{\Lambda}{\tilde{\Lambda}} + \frac{1}{f_b \tilde{\Lambda}} \right) \left(\frac{\Lambda}{\tilde{\Lambda}} + \frac{1}{f_a \tilde{\Lambda}} \right) < 1$$

(38)

Table 2. Square of the frequencies of the eigenmodes of the S2M system, equations (26), linearized around the trivial stationary points, $z_i^0 = 0$ for the four different $\delta\phi_i^0$ combinations.

$(\delta\phi_a^0, \delta\phi_b^0)$	ω_1^2/ω_R^2	ω_2^2/ω_R^2
$(0, 0)$	$1 + \dfrac{\Lambda}{2}\left(1 + \sqrt{(f_a - f_b)^2 + 4f_a f_b(\tilde{\Lambda}/\Lambda)^2}\right)$	$1 + \dfrac{\Lambda}{2}\left(1 - \sqrt{(f_a - f_b)^2 + 4f_a f_b(\tilde{\Lambda}/\Lambda)^2}\right)$
(π, π)	$1 - \dfrac{\Lambda}{2}\left(1 - \sqrt{(f_a - f_b)^2 + 4f_a f_b(\tilde{\Lambda}/\Lambda)^2}\right)$	$1 - \dfrac{\Lambda}{2}\left(1 + \sqrt{(f_a - f_b)^2 + 4f_a f_b(\tilde{\Lambda}/\Lambda)^2}\right)$
$(\pi, 0)$	$1 + \dfrac{\Lambda}{2}\left((f_b - f_a) + \sqrt{1 - 4f_a f_b(\tilde{\Lambda}/\Lambda)^2}\right)$	$1 + \dfrac{\Lambda}{2}\left((f_b - f_a) - \sqrt{1 - 4f_a f_b(\tilde{\Lambda}/\Lambda)^2}\right)$
$(0, \pi)$	$1 + \dfrac{\Lambda}{2}\left((f_a - vf_b) + \sqrt{1 - 4f_a f_b(\tilde{\Lambda}/\Lambda)^2}\right)$	$1 + \dfrac{\Lambda}{2}\left((f_a - f_b) - \sqrt{1 - 4f_a f_b(\tilde{\Lambda}/\Lambda)^2}\right)$

Table 3. The same as table 2 but retaining up to the first order in β, where $\tilde{\Lambda} = \Lambda(1 + \beta)$. We assume $f_a > f_b$.

$(\delta\phi_a, \delta\phi_b)$	ω_1^2/ω_R^2	ω_2^2/ω_R^2
$(0, 0)$	$1 + \Lambda(1 + 2\beta f_a f_b)$	$1 - 2\Lambda\beta f_a f_b$
(π, π)	$1 + 2\Lambda\beta f_a f_b$	$1 - \Lambda(1 + 2\beta f_a f_b)$
$(\pi, 0)$	$1 - \dfrac{2\beta f_a f_b \Lambda}{f_a - f_b}$	$1 + (f_b - f_a)\Lambda + \dfrac{2\beta f_a f_b \Lambda}{f_a - f_b}$
$(0, \pi)$	$1 + (f_a - f_b)\Lambda - \dfrac{2\beta f_a f_b \Lambda}{f_a - f_b}$	$1 + \dfrac{2\beta f_a f_b \Lambda}{f_a - f_b}$

guarantees the existence of two additional solutions in addition to the trivial one. However, in the particular case $\tilde{\Lambda} \sim \Lambda > 0$, the condition (38) cannot be fulfilled and therefore the only stationary point is the trivial one, $z_a^0 = z_b^0 = 0$.

In this case, the insertion of the stationary point, $z_a^0 = z_b^0 = 0$ and $\delta\phi_a^0 = \delta\phi_b^0 = 0$, into equation (37) yields

$$\Omega^2 = \omega_R^2 \begin{pmatrix} 1 & 0 \\ 0 & 1 \end{pmatrix} + \omega_R^2 \begin{pmatrix} f_a\Lambda & f_a\tilde{\Lambda} \\ f_b\tilde{\Lambda} & f_b\Lambda \end{pmatrix}, \tag{39}$$

which has two eigenvalues, listed in table 2.

In a very polarized mixture, $f_a \sim 1$, $f_b \sim 0$, the population imbalance of the most populated component decouples from the less populated one and oscillates with the Josephson frequency $w_J = \omega_1$ (see equation (26)). The less populated component is driven by the other component and follows its dynamics, thus giving rise to 'anti-Josephson' oscillations. The smaller frequency oscillation observed in the population imbalance of the less populated component is ω_2 (figure 13(a)), which is very similar to ω_R [36].

Also interesting is the non-polarized mixture, $f_a = f_b = 1/2$; then (assuming $\tilde{\Lambda} \sim \Lambda$, which is the case for ^{87}Rb),

$$\ddot{z_a}(t) = -\Lambda/2(z_a(t) + z_b(t)) - z_a(t),$$
$$\ddot{z_b}(t) = -\Lambda/2(z_a(t) + z_b(t)) - z_b(t), \tag{40}$$

and defining $\Delta z(t) = z_a(t) + z_b(t)$, $\delta z(t) = z_a(t) - z_b(t)$, we have

$$\ddot{\Delta z}(t) = -(\Lambda + 1)\Delta z(t), \quad \ddot{\delta z}(t) = -\delta z(t).$$

Therefore, Δz behaves as a single component, oscillating with the usual Josephson frequency, $w_J = \omega_R\sqrt{1+\Lambda}$, while δz oscillates with the Rabi frequency, as would a single component in the absence of atom–atom interactions. This mode can be further enhanced by imposing that $z_a(0) = -z_b(0)$, thus forcing both imbalances to oscillate with the same frequency.

We have proposed in [36] to use these two configurations to extract the frequencies governing the dynamics of the system in order to obtain the microscopic atom–atom interaction. The idea was to profit from the fact that the difference between the inter- and intra-species interactions is small for the case of ^{87}Rb, $\tilde{\Lambda} = \Lambda(1+\beta)$, so we can use the expressions listed in table 3, $\omega_1^2 = \omega_R^2(1 + \Lambda(1 + 2\beta f_a f_b))$ and $\omega_2^2 = \omega_R^2(1 - 2\Lambda\beta f_a f_b)$. Note that in the anti-Josephson case the oscillation with larger period is $\omega_2^2 = \omega_R^2(1 + \mathcal{O}(\beta f_b))$ and the shorter is $\omega_1^2 = \omega_R^2(1 + \Lambda + \mathcal{O}(\beta f_b))$, with $\beta \ll 1$ and $f_b \ll 1$, allowing us to extract both the Rabi and Josephson frequencies with good precision. The second configuration only has one frequency, which is $\omega_1^2 = \omega_R^2(1 + \Lambda(1 + \beta/2))$, which allows us to isolate the value of β.

3.6.2. Stationary points with $(\delta\phi_a^0 = \pi, \delta\phi_b^0 = 0)$. In this case, the condition for the existence of three stationary points is

$$\left(\frac{\Lambda}{\tilde{\Lambda}} - \frac{1}{f_a\tilde{\Lambda}}\right)\left(\frac{\Lambda}{\tilde{\Lambda}} + \frac{1}{f_b\tilde{\Lambda}}\right) > 1. \tag{41}$$

For the case considered here, $\tilde{\Lambda} \sim \Lambda$ and, in most applications, $\Lambda > 1$. Therefore, an appropriate choice of f_a can ensure the existence of three stable points.

The stability of the trivial solution is checked by studying

$$\Omega^2 = \omega_R^2\begin{pmatrix} 1 & 0 \\ 0 & 1 \end{pmatrix} + \omega_R^2\begin{pmatrix} f_a\Lambda & f_a\tilde{\Lambda} \\ -f_b\tilde{\Lambda} & -f_b\Lambda \end{pmatrix}, \tag{42}$$

whose eigenvalues are listed in table 2. The stability of the other two solutions is easy to study with the same tools. Simple analytic expressions are only attainable for the case $\tilde{\Lambda} = \Lambda$. Then we have

$$\Omega^2 = \omega_R^2\begin{pmatrix} 1 + \Lambda(f_a z_a^0 + f_b z_b^0)^2 & 0 \\ 0 & 1 + \Lambda(f_a z_a^0 + f_b z_b^0)^2 \end{pmatrix}$$

$$+ \omega_R^2\Lambda\begin{pmatrix} f_a\sqrt{1-(z_a^0)^2} & f_a\sqrt{1-(z_a^0)^2} \\ -f_b\sqrt{1-(z_b^0)^2} & -f_b\sqrt{1-(z_b^0)^2} \end{pmatrix}, \tag{43}$$

whose eigenvalues are

$$\omega_1^2 = \omega_R^2(\Lambda^2(f_a z_a^0 + f_b z_b^0)^2), \quad \omega_2^2 = \omega_R^2(1 + \Lambda^2(f_a z_a^0 + f_b z_b^0)^2). \tag{44}$$

3.6.3. Stationary points with $(\delta\phi_a^0 = \pi, \delta\phi_b^0 = \pi)$. The condition for the existence of three stationary points is in this case [27]

$$\left(\frac{\Lambda}{\tilde{\Lambda}} - \frac{1}{f_b\tilde{\Lambda}}\right)\left(\frac{\Lambda}{\tilde{\Lambda}} - \frac{1}{f_a\tilde{\Lambda}}\right) < 1. \tag{45}$$

IOP Institute of Physics ⏀DEUTSCHE PHYSIKALISCHE GESELLSCHAFT

The eigenvalues corresponding to small oscillations around the trivial point are listed in table 2. Its dynamical stability depends on the specific values of f_i, $\tilde{\Lambda}$, Λ and ω_R. For the case $\tilde{\Lambda} = \Lambda$, it is stable provided that $\omega_R > \Lambda$.

The eigenfrequencies for the non-trivial solution are the same as for the case ($\delta\phi_a = 0$, $\delta\phi_b = \pi$). For the simplest case, $\tilde{\Lambda} = \Lambda$, they are

$$\omega_1^2 = \omega_R^2 \left(\Lambda^2 \left(f_a z_a^0 + f_b z_b^0 \right)^2 \right), \quad \omega_2^2 = \omega_R^2 \left(1 + \Lambda^2 \left(f_a z_a^0 + f_b z_b^0 \right)^2 \right). \tag{46}$$

4. Effective one-dimensional (1D) mean field approaches

In the experimental realization [4] the condensate is confined by an asymmetric harmonic trap, characterized by ω_x, ω_y and ω_z, with a barrier on the x-direction. Thus, in a first approximation, one can assume that the dynamics takes place mostly along the x-axis and derive descriptions of the system where the other two dimensions have been integrated out reducing the GP3D equation to an effective 1D equation. There are different procedures for deriving effective 1D GP-like equations starting from the 3D one. Their generalization to binary mixtures, with two coupled GP equations, or spinor BEC, with three or more coupled GP equations, is presented below together with the single component case.

4.1. 1D Gross–Pitaevskii-like equations (GP1D)

Assuming that most of the dynamics occurs in the direction that contains the barrier, the x-direction in our case, one can approximate the wave function of the system by

$$\Psi(x, y, z; t) \sim \Psi^{1D}(x; t)\, \varphi_{g.s.}(y)\, \varphi_{g.s.}(z), \tag{47}$$

where $\varphi_{g.s.}$ are the corresponding ground state wave functions for the trapping potential in the y- or z-direction in the absence of interactions (in the case of harmonic traps they are Gaussian). In this way, it can be shown [41] that $\Psi^{1D}(x; t)$ fulfills a GP1D equation,

$$i\hbar \frac{\partial \Psi^{1D}(x; t)}{\partial t} = \left[-\frac{\hbar^2}{2m} \partial_x^2 + V(x) + g_{1D} N |\Psi^{1D}(x; t)|^2 \right] \Psi^{1D}(x; t), \tag{48}$$

where the corresponding 1D coupling constant is obtained rescaling the 3D one, $g_{1D} = g/(2\pi a_\perp^2)$, with $a_\perp$ being the transverse oscillator length, $a_\perp = \sqrt{\hbar/m\omega_\perp}$, with $\omega_\perp = \sqrt{\omega_z \omega_y}$.

The extension to binary mixtures (and also to spinor condensates [42]) may be written down readily,

$$i\hbar \frac{\partial \Psi_a^{1D}(x; t)}{\partial t} = \left[-\frac{\hbar^2}{2m} \partial_x^2 + V(x) + \sum_{j=a,b} g_{a\,j;1D} N_j |\Psi_j^{1D}(x; t)|^2 \right] \Psi_a^{1D}(x; t),$$

$$i\hbar \frac{\partial \Psi_b^{1D}(x; t)}{\partial t} = \left[-\frac{\hbar^2}{2m} \partial_x^2 + V(x) + \sum_{j=a,b} g_{b\,j;1D} N_j |\Psi_j^{1D}(x; t)|^2 \right] \Psi_b^{1D}(x; t), \tag{49}$$

where the rescaled couplings are $g_{ij;1D} = g_{ij}/(2\pi a_\perp^2)$.

4.2. Non-polynomial Schrödinger equation (NPSE)

A more sophisticated reduction that includes to some extent the transverse motion of the elongated BEC in the corresponding potential is the so-called NPSE, proposed for a scalar BEC in [26]. The NPSE recovers the previously discussed 1D reduction in the weakly interacting limit, but it has been shown to provide the best agreement with the experimental results on Josephson oscillations between two coupled BECs [25]. The NPSE for the scalar case reads

$$i\hbar \frac{\partial \Psi(x;t)}{\partial t} = \left[-\frac{\hbar^2}{2m} \partial_x^2 + V(x) + g_{1D} \frac{N|\Psi(x;t)|^2}{\sqrt{1 + 2a_s N|\Psi(x;t)|^2}} \right.$$

$$\left. + \frac{\hbar\omega_\perp}{2} \left(\frac{1}{\sqrt{1 + 2a_s N|\Psi(x;t)|^2}} + \sqrt{1 + 2a_s N|\Psi(x;t)|^2} \right) \right] \Psi(x;t). \qquad (50)$$

The generalization of the NPSE for two components in a binary mixture of BECs has been addressed in [43]. The system of equations, which become rather involved, can be greatly simplified in the case when all the interactions, both intra- and inter-species, are equal:

$$i\hbar \frac{\partial \Psi_j(x;t)}{\partial t} = \left[-\frac{\hbar^2}{2m_j} \partial_x^2 + V + g_{1D} \frac{\rho(x;t)}{\sqrt{1 + 2a_s \rho(x;t)}} \right.$$

$$\left. + \frac{\hbar\omega_\perp}{2} \left(\frac{1}{\sqrt{1 + 2a_s \rho(x;t)}} + \sqrt{1 + 2a_s \rho(x;t)} \right) \right] \Psi_j(x;t) \qquad (51)$$

where $\rho(x;t) = N_a|\Psi_a(x;t)|^2 + N_b|\Psi_b(x;t)|^2$, $j = a, b$ and, as before, $g_{1D} = g/(2\pi a_\perp^2)$, $g \equiv g_{aa} = g_{bb} = g_{ab} = g_{ba}$ and $\int dx |\Psi_j(x)|^2 = 1$.

5. Numerical solutions of the 3D GP equation: a single component

Before analyzing the binary mixtures in the next section, we will present here numerical results for the single component to illustrate the main differences between the various two-mode models and 1D reductions.

As discussed in the introduction, we consider the same setup and the same trap parameters as in the experiments of the Heidelberg group [4]. There, a condensate of ^{87}Rb with 1150 atoms is confined to a fairly small region of $\sim 5\,\mu$m through the potential

$$V(\mathbf{r}) = \frac{1}{2}M(\omega_x^2 x^2 + \omega_y^2 y^2 + \omega_z^2 z^2) + V_0 \cos^2(\pi x/q_0) \qquad (52)$$

with $\omega_x = 2\pi \times 78\,$Hz, $\omega_y = 2\pi \times 66\,$Hz, $\omega_z = 2\pi \times 90\,$Hz, $q_0 = 5.2\,\mu$m and $V_0 = 413\,h$ Hz. In figure 5, we show the potential in the x-direction together with the first four energy levels of the single particle Hamiltonian and the corresponding modes. The energy levels of the single particle Hamiltonian show a clear separation between the two first eigenvalues, ground and first excited states, which are almost degenerate, and the next two. As stated in section 3, the existence of this gap supports the validity of the two-mode approach.

The atom–atom interaction strength is, in this case, $g = 4\pi\hbar^2 a/M$. The scattering length for ^{87}Rb is $a = 100.87a_B$; therefore $g/\hbar = 0.04878\,$kHz μm^3. Noting that the number of atoms is known up to 10% in the experiment, the relevant product, $gN/\hbar$, is in the range [51.22, 60.98] kHz μm^3. The paper [14] uses a value of 58.8 kHz μm^3 to simulate the experimental setup. This
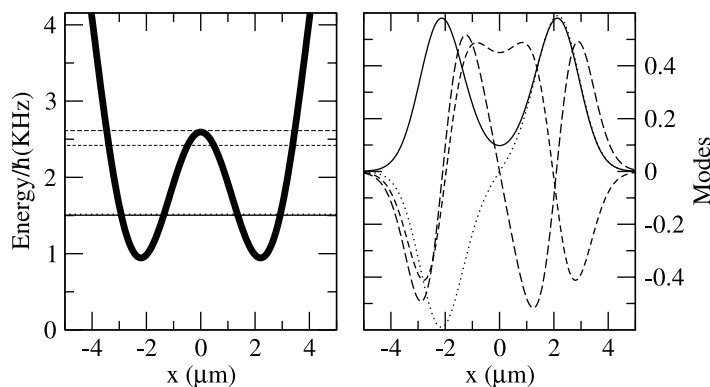
Figure 5. (Left) Depiction of the potential in the x-direction in units of $\hbar$. The horizontal lines correspond to the single particle eigenenergies of the single particle Hamiltonian. (Right) The first four single particle modes corresponding to the energies depicted on the left.

large value of gN corresponds to a situation similar to panel (c) of figure 4, where the possible dynamical situations are: Josephson oscillations, i.e. closed orbits around the stationary point $(z^0, \delta\phi^0) = (0, 0)$, and self-trapping regimes, usually running phase modes.

In the experiments, the system is prepared in a slightly uneven double-well potential, which produces an initial population imbalance between both sides of the barrier. At $t = 0$ the asymmetry is removed and the BEC is left to evolve in a symmetric double-well potential. In our numerical simulations, the initial states with either $\delta\phi(0) = 0$ or π are constructed in a different way from in the experiment. We build initial states that are by construction two mode like. First, we obtain numerically the ground and first excited states of the condensate in the double-well potential by solving the time-independent GP equation (both for the 1D reductions and the 3D case), then use those to build the left and right modes, equation (4), and finally construct initial states of any given initial imbalance, z_0: $\Psi_{z_0}(\mathbf{r}; t = 0) = \alpha\phi_L(\mathbf{r}) + e^{l_1\pi}\beta\phi_R(\mathbf{r})$, with $\alpha^2 + \beta^2 = 1$, $\alpha^2 - \beta^2 = z_0$ and $l = 0, 1$. The ground and first excited states are obtained by a standard imaginary time evolution of the equation from an initial state with the proper parity. The density profiles of the ground, first excited and left and right modes computed numerically are plotted in figure 1. As can be seen, the left/right modes are indeed well localized at each side of the barrier.

From these ground and first excited states we compute all the parameters entering the S2M and I2M descriptions presented in sections 3.1 and 3.2. The actual values of the parameters are $K/\hbar = 0.00799$ kHz and $NU/\hbar = 1.19841$ kHz for the S2M and $A/\hbar = 1.19372$ kHz, $B/\hbar = 0.03683$ kHz and $C/\hbar = 0.0023590$ kHz for the I2M[10]. The small value of C implies that the main difference between the I2M and S2M is not due to the term proportional to C in equation (13), which would imply qualitative differences between both, but mostly to a change in the tunneling rate due to the extra overlaps included in computing B in I2M.

The values of the overlaps are $N\gamma_{++}/\hbar = 0.581\,746$ kHz, $N\gamma_{+-}/\hbar = 0.598\,03$ kHz and $N\gamma_{--}/\hbar = 0.623\,769$ kHz. These numbers are used to generate the comparisons to S2M or I2M in the following figures.

[10] These values compare reasonably well with the ones provided on page 33 of Albiez's PhD thesis [25]; there they are given in units of ω_x: $A/\omega_x = 2.43572$, $B/\omega_x = 0.0751497$, $C/\omega_x = 0.0048$ and $K/\omega_x = 0.0163$.

In the full GP3D simulations, we define the number of atoms in the left well as $N_{\rm L}(t) = \int_{-\infty}^{0} {\rm d}x \int_{-\infty}^{\infty} {\rm d}y \int_{-\infty}^{\infty} {\rm d}z \, |\Psi(\mathbf{r}; t)|^2$. The number of atoms in the right well is computed as $N_{\rm R}(t) = N - N_{\rm L}(t)$. From these values, the population imbalance reads $z(t) = (N_{\rm L}(t) - N_{\rm R}(t))/N$. Analogous definitions are used in the GP1D and NPSE equations.

The phase difference between both sides of the potential barrier is computed in the following way. The phase at each point at a certain time, $\phi(x, y, z; t)$, is

$$\Psi(x, y, z; t) = \sqrt{\rho(x, y, z; t)} \exp(\iota \, \phi(x, y, z; t)), \tag{53}$$

where the local density, $\rho(x, y, z; t) = |\Psi(x, y, z; t)|^2$.

Averaged densities are defined as, i.e. integrating over the z-component,

$$\rho(x, y; t) = \int_{-\infty}^{\infty} {\rm d}z \, \rho(x, y, z; t). \tag{54}$$

To visualize the phase coherence along some of the planes, we define an average phase, e.g. integrating the z-component,

$$\phi(x, y; t) = \frac{1}{\rho(x, y; t)} \int_{-\infty}^{\infty} {\rm d}z \, \rho(x, y, z; t) \, \phi(x, y, z; t). \tag{55}$$

The phase on the left, $\phi_{\rm L}(t)$, is defined as

$$\phi_{\rm L}(t) = \frac{1}{N_{\rm L}(t)} \int_{-\infty}^{0} {\rm d}x \int_{-\infty}^{\infty} {\rm d}y \int_{-\infty}^{\infty} {\rm d}z \, \rho(x, y, z; t) \, \phi(x, y, z; t). \tag{56}$$

The phase on the right is defined accordingly.

The way to implement the above averages over the phase has been done in the following way:

$$\phi(x, y; t) = \arctan \frac{\int_{-\infty}^{\infty} {\rm d}z \, {\rm Im}[\Psi(x, y, z; t)] \, \rho(x, y, z; t)}{\int_{-\infty}^{\infty} {\rm d}z \, {\rm Re}[\Psi(x, y, z; t)] \, \rho(x, y, z; t)},$$

$$\phi_{\rm L}(t) = \arctan \frac{\int_{-\infty}^{0} {\rm d}x \int_{-\infty}^{\infty} {\rm d}y \int_{-\infty}^{\infty} {\rm d}z \, {\rm Im}[\Psi(x, y, z; t)] \, \rho(x, y, z; t)}{\int_{-\infty}^{0} {\rm d}x \int_{-\infty}^{\infty} {\rm d}y \int_{-\infty}^{\infty} {\rm d}z \, {\rm Re}[\Psi(x, y, z; t)] \, \rho(x, y, z; t)}. \tag{57}$$

5.1. GP3D results

In figures 6 and 7, we present full GP3D simulations for a Josephson regime and a running phase mode self-trapped case, respectively. These figures clearly show two relevant aspects of the problem. Firstly, it is clear that during the full time evolution, which covers up to $t = 80$ ms in the figure, the system remains mostly localized on the two minima of the potential. Therefore, the density has a two-peaked structure over the considered time period. Secondly, the atoms in each of the two wells remain to a large extent in a coherent phase at all times. This can be seen from the uniform color, constant phase, on each side of the barrier in the right panels of the figures. These two characteristics of the time evolution of the 3DGP equation support the use of two-mode approximations.

The modulation of the density profiles on the transverse direction is seen to be small, with a mostly constant quantum phase in the region populated by the atoms. This indicates that the transverse dynamics can be integrated out to a large extent, as is done in the 1D reductions discussed in section 4.
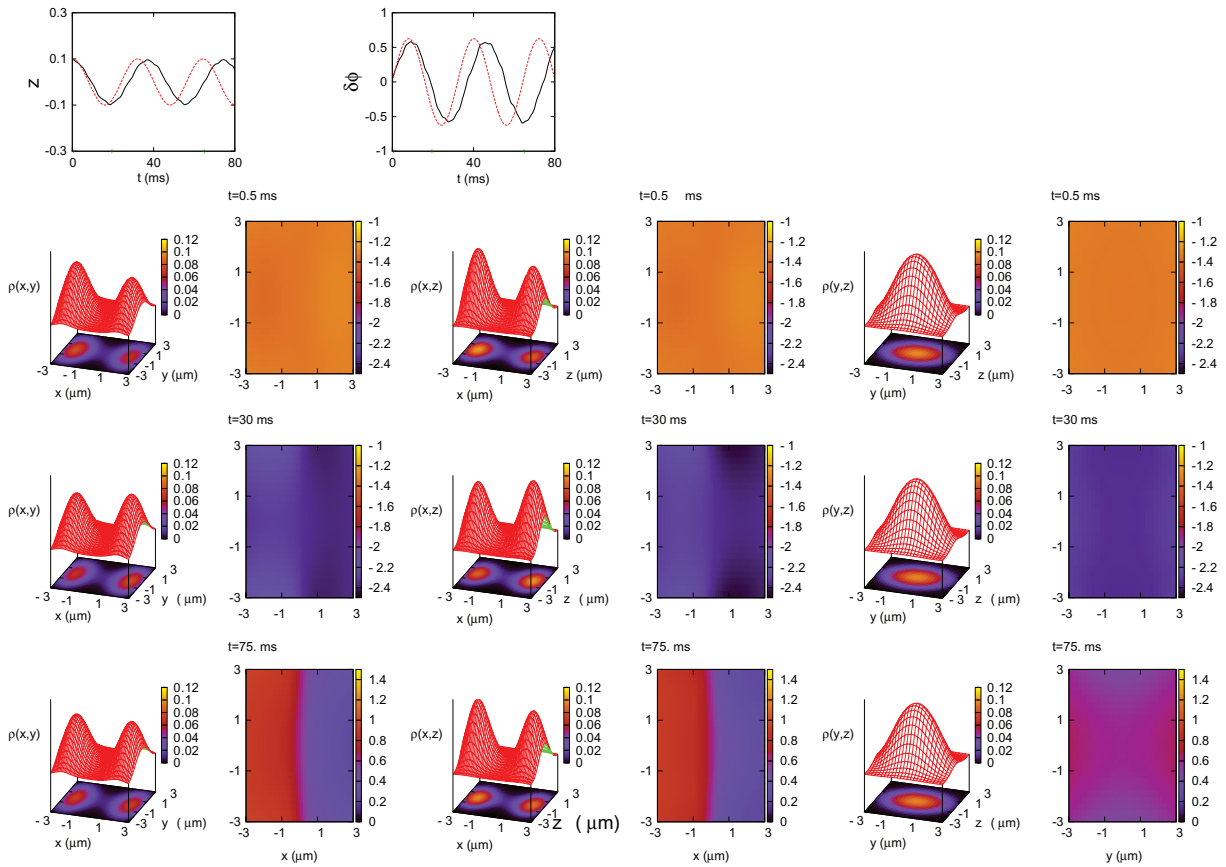
Figure 6. The two smaller plots above depict in solid black line the GP3D time evolution of z (left) and $\delta\phi$ (right), computed as explained in the text compared with the I2M predictions in dashed red. Then we show 3D pictures complemented with contour plots, left, of $\rho(x, y; t)$, $\rho(x, z; t)$ and $\rho(y, z; t)$ at three different times, 0.5 ms (top), 30 ms (middle) and 75 ms (bottom), respectively. On the right of each plot, we present a contour plot of the averaged quantum phase $\phi(x, y; t)$, $\phi(x, z; t)$ and $\phi(y, z; t)$ at the same times. They correspond to the first run presented in figure 8(a), $z(0) = 0.1$ and $\delta\phi(0) = 0$.

The Josephson dynamics, figure 6, is clearly seen in the small upper panels depicting $z(t)$ and $\delta\phi(t)$. They both oscillate with the same period but with a phase shift of $\pi/2$.

A self-trapped case is shown in figure 7. The atoms remain trapped mostly on the left side of the trap (they start with an imbalance of $z(0) = 0.7$) and remain trapped in this potential well during the considered time evolution. The coherence of the phase on each side of the potential barrier can also be appreciated in the figure, although here we should note that the right side of the barrier, being less populated, is concentrated on a smaller (x, y) domain.

5.2. Comparison between the different models

The GP3D cases described above indicate that within the configuration considered here the two commonly employed two-mode models and 1D equations are expected to be reasonable. In this
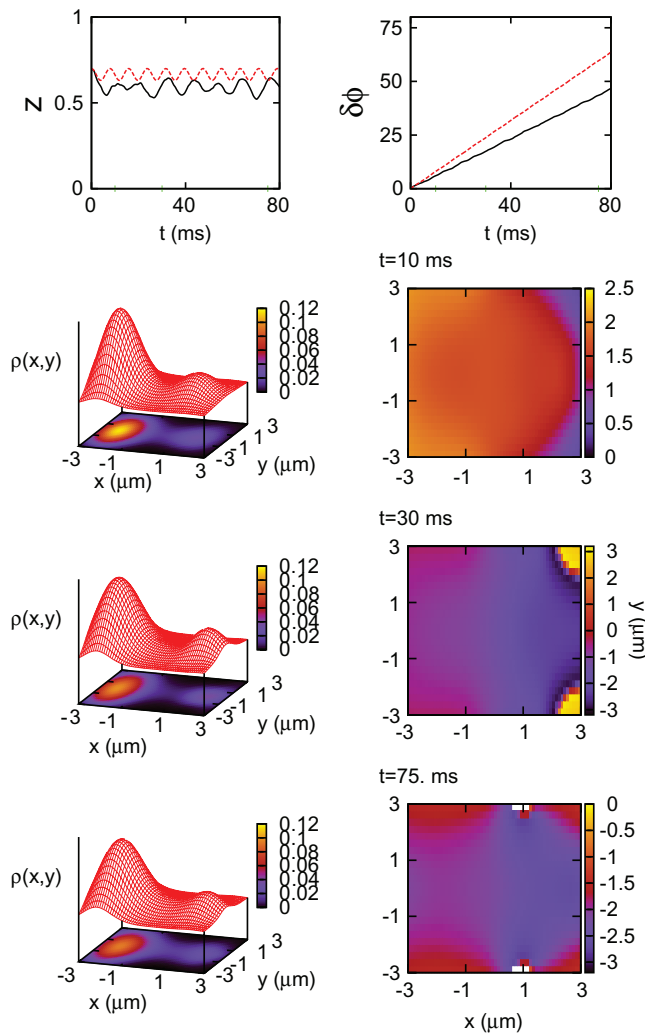
Figure 7. Similar to figure 6 but for a self-trapped case, $z(0) = 0.7$, $\delta\phi(0) = 0$, for three different times, 10, 30 and 75 ms and showing the averages over z. We plot $\rho(x, y; t)$ and contour plots. In the right panels, we present contour plots of the averaged quantum phase, $\phi(x, y; t)$. The phase coherence of the condensates on each side of the barrier is clearly seen.

section, we present comparisons between the different approaches described in the previous sections: 1D reductions (NPSE and GP1D) and two-mode models, S2M and I2M.

5.2.1. GP3D versus 1D reductions: GP1D and NPSE. In figure 8, we present the time evolution of the population imbalance for the different dynamical regimes described in section 3.3, i.e. Josephson and self-trapping. We compare the full GP3D (solid red) with the two previously described 1D reductions, GP1D (dotted black) and NPSE (dashed blue).

First, we note that the dynamics emerging from the GP3D is indeed similar to what was predicted by analyzing the S2M equations in section 3.3. Qualitatively, the GP3D simulations follow the patterns predicted by the two-mode approximations. Lets us briefly describe each of

IOP Institute of Physics ⓓ DEUTSCHE PHYSIKALISCHE GESELLSCHAFT
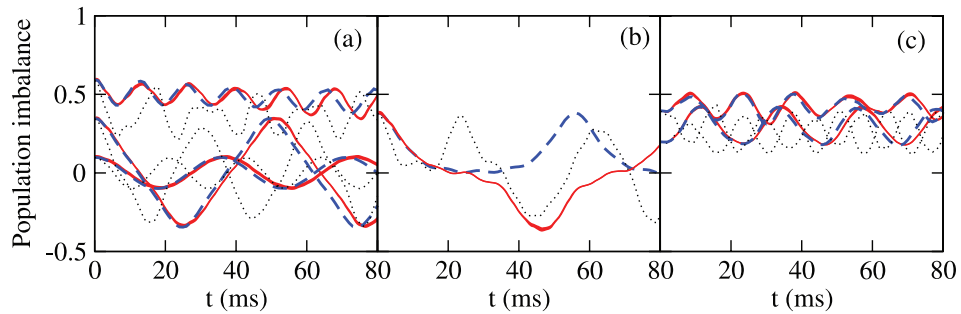
Figure 8. Dynamical evolution of the population imbalance, z, between both sides of the barrier for a single component condensate. Solid (red) line corresponds to the GP3D, the dashed (blue) line to the NPSE and the dotted (black) stands for the GP1D. Panel (a) contains $\delta\phi(0) = 0$ cases, with $z(0) = 0.1, 0.35$ and 0.6. Panel (b) corresponds to the critical value, $z(0) = 0.39$ and $\delta\phi(0) = 0$. Panel (c) depicts two self-trapped cases with an initial $\delta\phi(0) = \pi$, with $z(0) = 0.2$ and 0.4.

the results:

(a) The first panel, (a), contains simulations performed with zero initial phase difference, i.e. Josephson oscillations and self-trapping cases. For the Josephson cases, $z(0) = 0.1, 0.35$, the imbalance oscillates with a frequency that is mostly independent of the initial imbalance (for small imbalances). With $z(0) = 0.1$ the oscillations are almost sinusoidal, while as we increase the initial imbalance their shape becomes more involved while remaining periodic. In the self-trapped case, $z(0) = 0.6$, the atoms remain mostly on the initial side of the trap and there are short and small periodic oscillations as predicted by the two-mode models. At longer times, the imbalance is seen to decrease smoothly, implying a departure from the predicted two-mode dynamics [44].

   The two 1D reductions give qualitatively similar results in most situations to GP3D, but not quantitatively in all cases. The NPSE is seen to reproduce very well the GP3D in all the runs up to times near ~ 40 ms. Above those times, the period of oscillation predicted by the NPSE is slightly shorter than the GP3D one. The GP1D, on the contrary, only captures the amplitude of oscillation in the Josephson dynamics, failing in all cases to give the same period as the GP3D or the NPSE. Moreover, the GP1D departs notably from two-mode for the self-trapped case. It does predict self-trapping, but more than two modes contribute to the time evolution.

(b) Panel (b) is computed very close to the critical value of the full GP3D, $z(0) = 0.39$ for $\delta\phi(0) = 0$. The GP1D and NPSE predict a critical initial imbalance close to the GP3D value.

(c) Panel (c) contains two self-trapped cases obtained with an initial $\delta\phi(0) = \pi$ and $z(0) = 0.2$ and 0.4. Note that for $\delta\phi(0) = \pi$ the critical imbalance is smaller than for $\delta\phi(0) = 0$. The discussion is similar to the Josephson case, i.e. the NPSE captures most of the dynamical features of the GP3D, while the GP1D only provides a qualitative understanding of the problem.
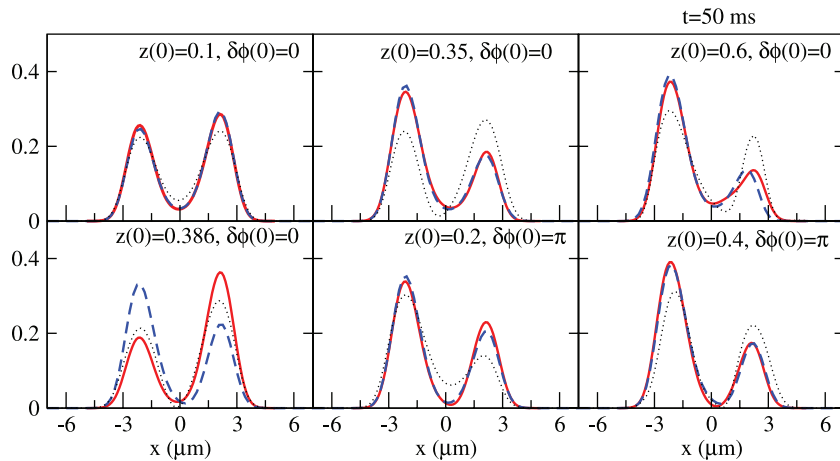
Figure 9. Snapshots of the axial density profiles, $\rho(x; t)$ $(\mu\text{m})^{-1}$ at $t = 50\,\text{ms}$, calculated by means of the GP3D evolution (solid red line), the NPSE (dashed blue line) and the GP1D (dotted black line). The initial conditions correspond to the ones used to generate figure 8.

To further explore the quality of the 1D reductions, we present in figure 9 the density profiles in the x-direction after integrating the y- and z-components, $\rho(x; t) = \int_{-\infty}^{\infty} dy \int_{-\infty}^{\infty} dz\, |\Psi(x, y, z; t)|^2$ at $t = 50\,\text{ms}$. The agreement between the NPSE and the GP3D is very good in most situations, except for the critical case, as expected. In all cases the density profiles show a clear bi-modal structure. The GP1D, as could be inferred from the previous results, does not predict the correct density profiles and, as seen in the self-trapped case, $(z(0) = 0.6, \delta\phi(0) = 0)$, does show the contribution of higher modes. The critical initial imbalance starting with no phase difference that we find numerically by means of the GP3D is the same as that found in [14], $z_c = 0.39$, and differs from the one reported in [4], $z_c = 0.5$.

The agreement of the NPSE with GP3D results justifies the use of NPSE in [4] to analyze their experiment.

5.2.2. GP3D versus two-mode approximations, S2M and I2M. As explained above, the use of two-mode models is suggested by the GP3D results, see figures 6 and 7. What is, *a priori*, not clear is whether the extra assumption used in deriving the S2M (which are the most commonly employed equations) will work for each specific double-well potential. As discussed in section 3.2, the conditions of the Heidelberg experiment are such that the S2M predictions are not good. However, this does not mean that the dynamics is not two-mode but that the overlaps involving high powers of the two localized modes are not negligible as assumed in deriving the S2M equations.

In figure 10, we compare GP3D (solid red), the S2M (dotted black) and the I2M (dashed blue) results using the parameters calculated microscopically from the ground and first excited states of the GP3D. Both two-mode schemes predict the same phenomenology and thus qualitatively capture the dynamics of the system. At the quantitative level, however, the I2M is clearly better. In the run with $z(0) = 0.1$ and $\delta\phi(0) = 0$ (panel (a)), both the S2M and I2M predict similar behavior with the correct amplitude and oscillation period close to the GP3D one. As the imbalance is increased, e.g. ([4] considers $z(0) = 0.28$), the S2M fails to describe the
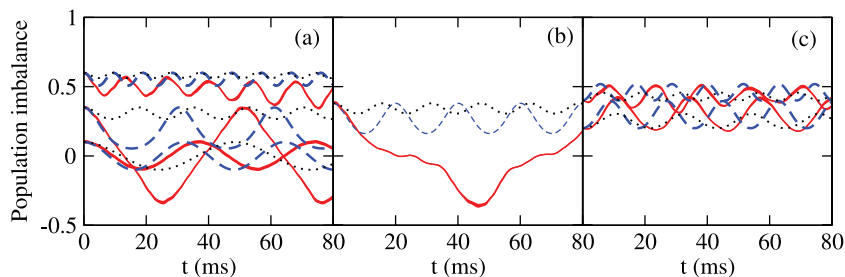
Figure 10. Dynamical evolution of the population imbalance between the two sides of the barrier for a single component condensate. The GP3D (solid red) is compared to the I2M (dashed blue) and the S2M (dotted black) results. The parameters entering the two-mode descriptions are given in the text. Panel (a) contains runs for $\delta\phi(0) = 0$, with $z(0) = 0.1, 0.35$ and 0.6. Panel (b) corresponds to the critical value for $z(0) = 0.39$ and $\delta\phi(0) = 0$. Panel (c) depicts two self-trapped states obtained by an initial $\delta\phi(0) = \pi$, with $z(0) = 0.2$ and 0.4.

correct period and predicts smaller amplitudes. This is analyzed in full detail in [14]. The critical initial imbalances determined by both two-mode approaches are smaller than the GP3D one, see panel (b). Finally, for the self-trapped cases with $\delta\phi(0) = \pi$ (panel (c)) the I2M gives similar oscillation amplitudes with shorter periods than the GP3D. The S2M fails both in reproducing the amplitudes and the periods.

6. Numerical solutions of the 3D GP equations: a binary mixture

As discussed in section 2, one feasible way of experimentally preparing binary mixtures of BECs is to consider a number of atoms populating the $m = \pm 1$ Zeeman components of an ^{87}Rb $F = 1$ spinor. The experimental observation of Josephson tunneling phenomena by the Heidelberg group seems to be possibly extended to trap both Zeeman components [40]. In this case, the two components of the mixture have the same mass, $M \equiv m_a = m_b$, and equal intra-species interactions, $g_{aa} = g_{bb} \equiv g$. With respect to the inter-species interaction we will consider the case of ^{87}Rb, which implies $g_{ab} \sim g$.

The mean field GP3D system of equations governing the dynamics of the three components of an $F = 1$ spinor BEC can be written as [45]

$$i\hbar \frac{\partial \psi_{\pm 1}}{\partial t} = [\mathcal{H}_s + c_2(n_{\pm 1} + n_0 - n_{\mp 1})]\psi_{\pm 1} + c_2\psi_0^2\psi_{\mp 1}^*,$$

$$i\hbar \frac{\partial \psi_0}{\partial t} = [\mathcal{H}_s + c_2(n_1 + n_{-1})]\psi_0 + c_2 2\psi_1\psi_0^*\psi_{-1},$$

(58)

with $\mathcal{H}_s = -\hbar^2/(2M)\nabla^2 + V + c_0 n$ being the spin-independent part of the Hamiltonian. The density of the mth component is given by $n_m(\mathbf{r}) = |\psi_m(\mathbf{r})|^2$, while $n(\mathbf{r}) = \sum_m |\psi_m(\mathbf{r})|^2$ is the total density normalized to the total number of atoms N. The couplings are $c_0 = 4\pi\hbar^2(a_0 + 2a_2)/(3M)$ and $c_2 = 4\pi\hbar^2(a_2 - a_0)/(3M)$, where a_0 and a_2 are the scattering lengths describing binary elastic collisions in the channels of total spin 0 and 2, respectively. Their values for ^{87}Rb are $a_0 = 101.8a_B$ and $a_2 = 100.4a_B$ [46]. Since the spin-dependent coupling, c_2, is much
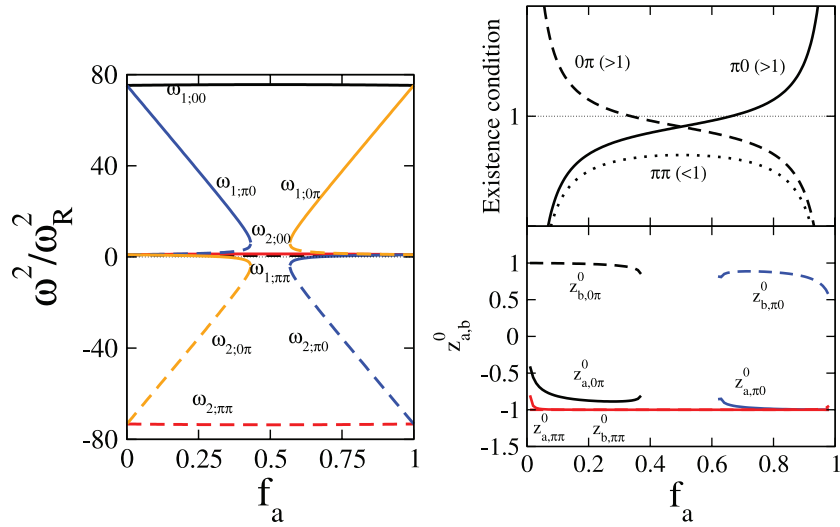
Figure 11. (Left) Values of the frequencies, ω/ω_R, listed in table 3 for the specific conditions considered in the numerical simulations as a function of the fraction of atoms in the a component, f_a. The notation is as follows: $\omega_{i;\alpha\beta}$, with $i = 1, 2$ being the index of the eigenfrequency and $\alpha, \beta = 0, \pi$ the phase difference of the stationary point for each component. (Right) The conditions for the existence of the non-trivial equilibrium points given in equations (38), (41) and (45), upper panel, as a function of f_a for the conditions described in the text. The lower panel contains the explicit equilibrium points z_a^0, z_b^0 as a function of f_a obtained by solving equations (34). Note that each equilibrium point has a trivial partner, which is obtained by flipping the sign of z_a^0, z_b^0.

smaller than the spin-independent one, c_0, and the total number of atoms that we will consider is relatively small $N = 1150$, the population transfer between the different components can be neglected [36]. Therefore, in our calculation the number of atoms in each sublevel remains constant in time, allowing us to treat the system as a binary mixture of components a and b. Comparing the system of equations (1) and (58) the value of the couplings can be read off, $g_{aa} = g_{bb} = c_0 + c_2$ and $g_{ab} = g_{ba} = c_0 - c_2$.

Once the total number of atoms is fixed we want to investigate the Josephson-like dynamics for different numbers of atoms populating each component $N_a = f_a N$ and $N_b = f_b N$ and for different initial conditions, $z_a(0)$, $z_b(0)$, $\delta\phi_a(0)$ and $\delta\phi_b(0)$.

The values of $\Lambda = NU/\hbar\omega_R$ and $\tilde{\Lambda} = N\tilde{U}/\hbar\omega_R$ are $\Lambda = 74.278$ and $\tilde{\Lambda} = 74.968$. With $\Lambda/\tilde{\Lambda} = 0.99$. These are obtained from the microscopic 3D parameters computed in the scalar case, with the same total number of particles, see section 5. This is reasonable for the case we are considering where $g_{aa} = g_{bb} \sim g_{ab}$, which implies that the ground state wave functions for the GP equations of the mixture do not depend on f_a and f_b for a fixed total number of particles. This would certainly not be the case if $g_{aa} = g_{bb} \neq g_{ab}$; in such case, one would need to recompute the ground state wave functions for a and b for each value of f_a.

Following the discussion in section 3.6, where the predictions of the S2M were discussed in detail, the system has the trivial equilibrium points, listed in table 3 with $\beta = 0.009$. In figure 11, we show the values of the two eigenfrequencies for each of the trivial equilibrium points listed in table 3 for the specific conditions described above. The figure shows a number of important

features about the stability of the trivial equilibrium points. Firstly, the $(z_a^0, \delta\phi_a^0, z_b^0, \delta\phi_b^0) = (0, 0, 0, 0)$ is always stable regardless of the total polarization of the system (measured by $f_b - f_a$). Secondly, the $(z_a^0, \delta\phi_a^0, z_b^0, \delta\phi_b^0) = (0, \pi, 0, \pi)$ mode is always unstable, as seen by the negative value taken by the square of the frequencies. Thirdly, the $(z_a^0, \delta\phi_a^0, z_b^0, \delta\phi_b^0) = (0, 0, 0, \pi)$ mode should be stable for $f_b \lesssim 0.43$, correspondingly the $(z_a^0, \delta\phi_a^0, z_b^0, \delta\phi_b^0) = (0, \pi, 0, 0)$ is stable for $f_a \lesssim 0.43$ and therefore there is a range of polarizations, given by $0.43 \lesssim f_a \lesssim 0.57$, where the only trivial mode that is stable is the $(z_a^0, \delta\phi_a^0, z_b^0, \delta\phi_b^0) = (0, 0, 0, 0)$.

The non-trivial equilibrium points in this case can be obtained by analyzing the conditions given in section 3.6. For $(\delta\phi_a^0, \delta\phi_b^0) = (0, 0)$ there are no equilibrium points apart from the trivial one, due to $\Lambda \sim \tilde{\Lambda}$. In the other three cases there are non-trivial equilibrium points depending on the specific values of f_a. In figure 11 (right) we analyze their existence. First, we note that there are non-trivial points corresponding to $(\delta\phi_a^0, \delta\phi_b^0) = (0, \pi)$ provided $f_a \lesssim 0.37$, correspondingly there are also equilibrium points for $(\delta\phi_a^0, \delta\phi_b^0) = (0, \pi)$ if $f_b \lesssim 0.37$. There is also a non-trivial equilibrium point for $(\delta\phi_a^0, \delta\phi_b^0) = (\pi, \pi)$ regardless of f_a. As can be seen in the figure, all these non-trivial equilibrium points correspond to fairly imbalanced conditions and can in most cases be understood in simple terms from the analysis of the scalar case. For instance, the equilibrium point for $(\delta\phi_a^0, \delta\phi_b^0) = (\pi, \pi)$ corresponds to $z_a^0 \sim z_b^0 \sim 1$ (or -1), which can be understood as having both components locked in a π-mode. Similarly, the equilibrium points in the $(0, \pi)$ or $(\pi, 0)$ cases exist whenever the most abundant component is populated enough to drive the dynamics close to being π locked.

6.1. GP3D calculations: phase coherence and localization

The numerical solutions of the GP3D presented in section 5 for the single component system showed two features. Firstly, the atoms remained mostly localized in the two minima of the potential well and, secondly, each group of atoms had to a large extent the same quantum phase. This clearly supported the picture of having two BECs, one on each side of the barrier, with a well-defined phase on each side during the dynamical evolution. Essentially those are the premises used to derive the two-mode models, both for single component and for binary mixtures, as we did in section 3.

As in the scalar case, our exact GP3D numerical solutions of the dynamics of the binary mixture in several initial conditions of population imbalances and phase differences show two distinctive features, see figure 12. Firstly, the density of atoms for each component is always bi-modal, with the two atom bunches centered around the minima of the potential well. Secondly, the phase of the wave function is mostly constant for each species on each side of the potential trap. Thus, we find that the GP3D does predict the dynamics to be mostly bi-modal also for the binary mixture case.

At the end of the section we will consider some deviations from the bi-modal behavior that are found in very specific conditions, e.g. for very large population imbalances and also when analyzing a case with $g_{ab} \neq g_{aa} = g_{bb}$.

6.2. Small oscillations around $z_{a,b}^0$ and $\delta\phi_{a,b}^0 = 0$

The two predictions of the two-mode described in section 3.6, namely the 'anti-Josephson' behavior and the enhancement of the Rabi mode, are confirmed by the NPSE and GP1D simulations as can be seen in figure 13. In figure 13 (left panels), we consider a very polarized case, $f_a = 0.8$. As expected from the two-mode analysis the dynamics of the most populated
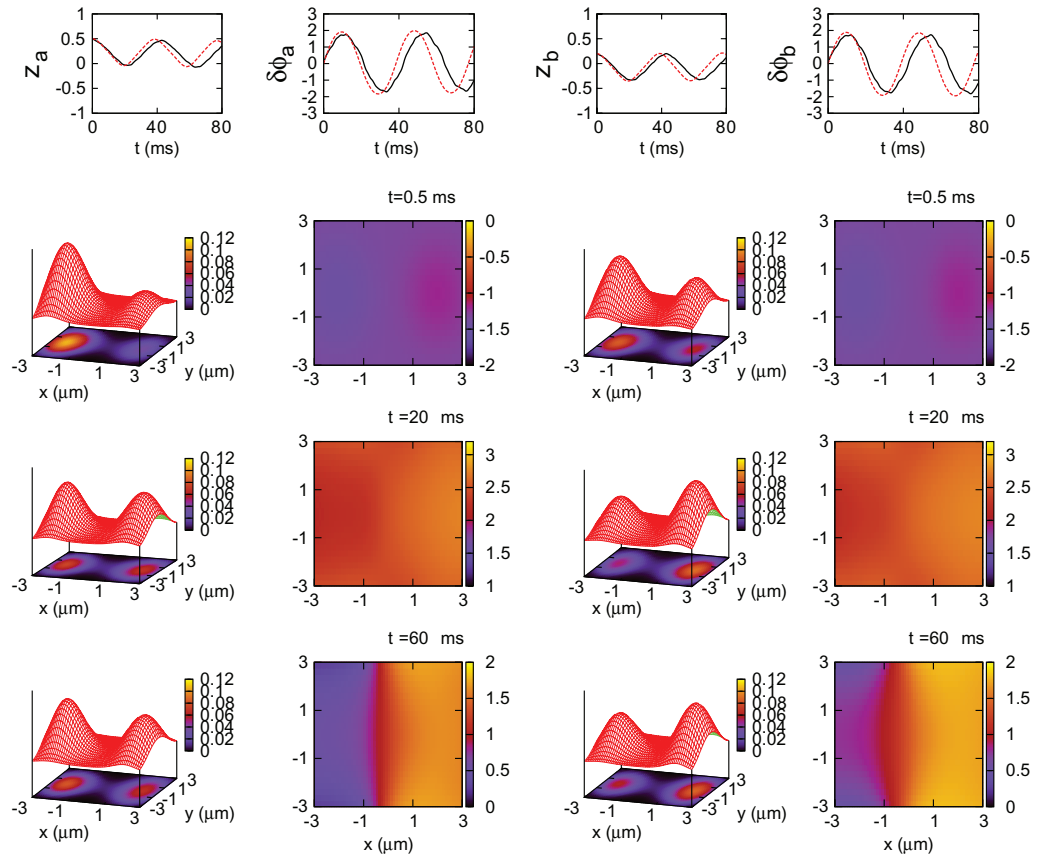
Figure 12. Full GP3D calculations of the dynamics of a binary mixture with $z_a(0) = 0.5$, $z_b(0) = 0.2$, $\delta\phi_a(0) = 0$, $\delta\phi_b(0) = 0$, $f_a = 0.25$ and $f_b = 0.75$. The upper four plots depict, from left to right, $z_a(t)$, $\delta\phi_a(t)$, $z_b(t)$ and $\delta\phi_b(t)$ in solid black compared to the I2M prediction, dashed red. Then each row contains from left to right: 3D depictions complemented by contour plots of $\rho_a(x, y; t)$, a contour plot of the averaged phase $\phi_a(x, y; t)$, 3D depictions complemented by contour plots of $\rho_b(x, y; t)$, and a contour plot of the averaged phase $\phi_b(x, y; t)$. Each row corresponds to a different time, 0.5 ms (upper), 20 ms (middle) and 60 ms (lower), respectively.

component should to a large extent decouple from the less populated one and perform fast Josephson oscillations with a frequency close to the corresponding one for the scalar case, $\omega_J = \omega_R\sqrt{1 + \Lambda}$. The GP3D simulation is seen to confirm the above and follow closely the predictions of the I2M. The less abundant component is strongly driven by the most populated one and shows anti-Josephson behavior as described in [36].

Another prediction is related to the behavior of $z_a + z_b$ and $z_a - z_b$ in the non-polarized case, $f_a = f_b$. As explained in section 3.6, in this case the difference, $z_a - z_b$, should enhance the long mode that oscillates with the Rabi frequency of the system, while the sum $z_a + z_b$ should mostly oscillate with the Josephson frequency. In the right part of figure 13 we present the extreme case when $z_a(0) = -z_b(0)$ computed with GP3D, NPSE and I2M. In this case, both population imbalances and phase differences oscillate mostly with the Rabi frequency of the system, keeping during the time evolution $z_a + z_b \sim 0$.
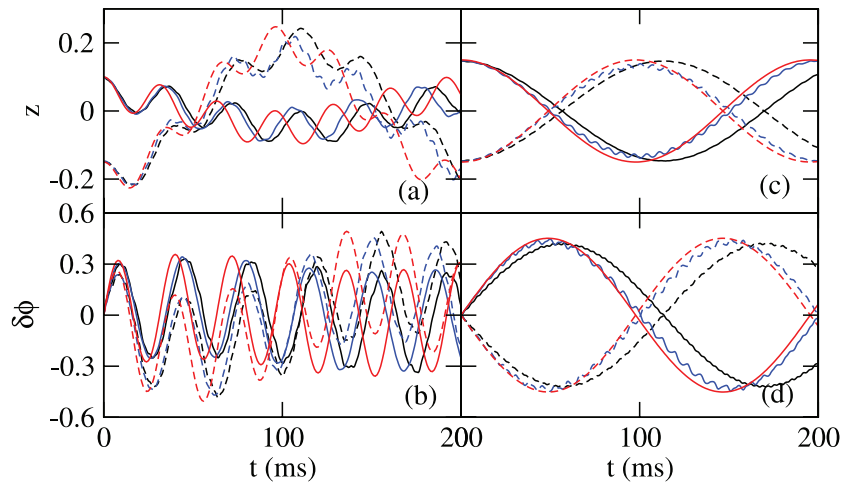
Figure 13. Behavior of the population imbalance, $z_a(t)$ (solid lines) and $z_b(t)$ (dashed lines) and phase difference, $\delta\phi_a(t)$ (solid lines) and $\delta\phi_b(t)$ (dashed lines), computed using GP3D (black lines), NPSE (blue lines) and I2M (red lines) in a polarized case, $f_a = 0.8$, left and a zero polarization case, $f_a = 0.5$, right, respectively. The initial conditions are $z_a(0) = 0.1$, $z_b(0) = -0.15$ and $\delta\phi_a(0) = \delta\phi_b(0) = 0$ for the left panels and $z_a(0) = -z_b(0) = 0.15$ and $\delta\phi_a(0) = \delta\phi_b(0) = 0$ for the right panels.
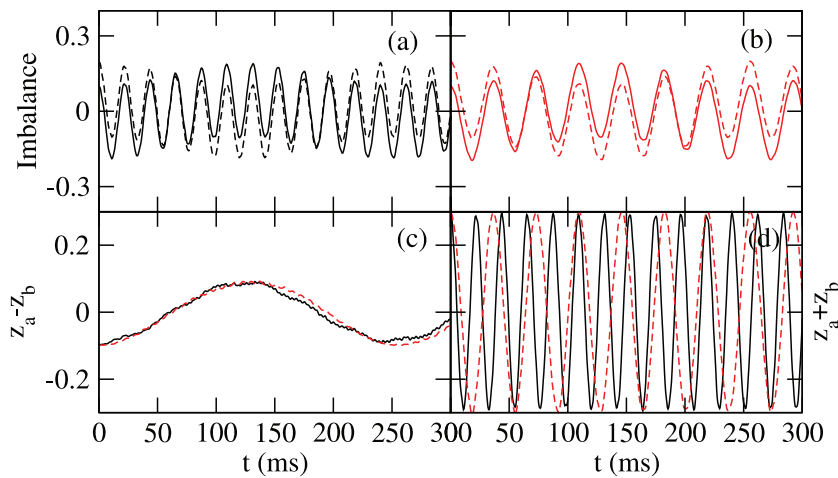
Figure 14. Behavior of the population imbalance in NPSE (red) and GP1D (black) simulations in the zero magnetization case, $f_a = f_b$. The initial conditions are $z_a(0) = 0.1$, $z_b(0) = 0.2$ and $\delta\phi(0) = 0$. The upper panels correspond to (a) $z_a(t)$ (solid line) and $z_b(t)$ (dashed line) obtained with the GP1D equations, (b) $z_a(t)$ and $z_b(t)$ obtained with the NPSE equations, (c) behavior of $z_a(t) - z_b(t)$ for GP1D (solid) and NPSE (dashed) and (d) behavior of $z_a(t) + z_b(t)$.

As seen in figure 14 both 1D reductions produce qualitatively similar physics. The only important difference is that the frequency of the Josephson oscillations is higher in the GP1D, as occurred already for the single component, see section 5.
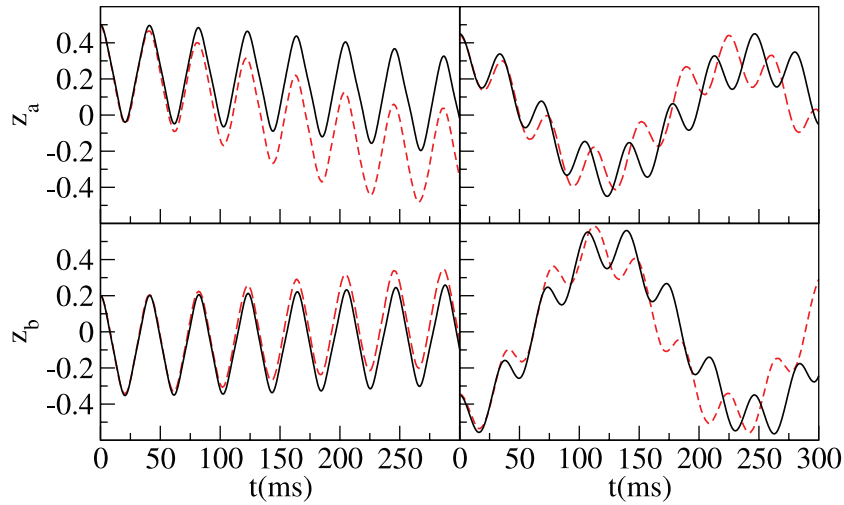
Figure 15. (Left panels) Evolution of the population imbalance of each component for a binary mixture with $f_a = 0.25$. The top panel shows $z_a(t)$, and the bottom panel $z_b(t)$. The solid (black) line corresponds to the I2M model and the dashed (red) line to the NPSE. The initial conditions are $z_a(0) = 0.5$, $z_b(0) = 0.2$, $\delta\phi_a(0) = \delta\phi_b(0) = 0$. (Right panels) As in the left panels, but with $f_a = 0.6$ and initial conditions $z_a(0) = 0.45$, $z_b(0) = -0.35$, $\delta\phi_a(0) = \delta\phi_b(0) = 0$.

Interestingly, they predict different Josephson oscillations while the Rabi frequencies are similar. In panel (c) of figure 14 the long oscillation corresponding to the Rabi mode is seen to agree well with the corresponding long oscillation seen in the right panels of figure 13. The Josephson-like oscillations of binary mixtures of spinor $F = 1$ ^{87}Rb BECs around the $(z_a^0, \delta\phi_a^0, z_b^0, \delta\phi_b^0) = (0, 0, 0, 0)$ are therefore essentially controlled by two frequencies, ω_R and ω_J.

As a general statement, in the conditions of the Heidelberg experiment, as occurred for the scalar case, the I2M produces more reliable results than the S2M model, which are not shown in the figures. Note that the parameters that we use for the I2M are extracted from the GP3D calculation as given in section 5. Other representative cases with $(\delta\phi_a(0), \delta\phi_b(0)) = (0, 0)$ but with larger initial imbalances, $z_i(0) \sim 0.5$, are shown in figure 15. On the left side of this figure we show the population imbalance of each component for a simulation with $f_a = 0.25$. In this case, the dynamics is controlled by ω_J. The panel on the right depicts a simulation with $f_a = 0.6$ and close to opposite initial population imbalances. In this case, both frequencies ω_J and ω_R show up in the evolution. The I2M provides a satisfactory description of the dynamics.

6.3. Small oscillations around $z_{a,b}^0$, $\delta\phi_a^0 = 0$ and $\delta\phi_b^0 = \pi$

As explained above, for these conditions there can exist up to three stationary points depending on the specific value of f_a considered. The trivial equilibrium point exists provided $f_a \lesssim 0.43$, see figure 11. This prediction of the two-mode models is observed in both the GP3D and the NPSE as can be seen in figure 16. In the figure, we consider a simulation with $z_a(0) = 0.1$, $z_b(0) = -0.15$ and $f_b = 0.2 < 0.43$ (left panels). The population imbalance (upper panel) of both components oscillates in the usual Josephson regime. At the same time, the phase
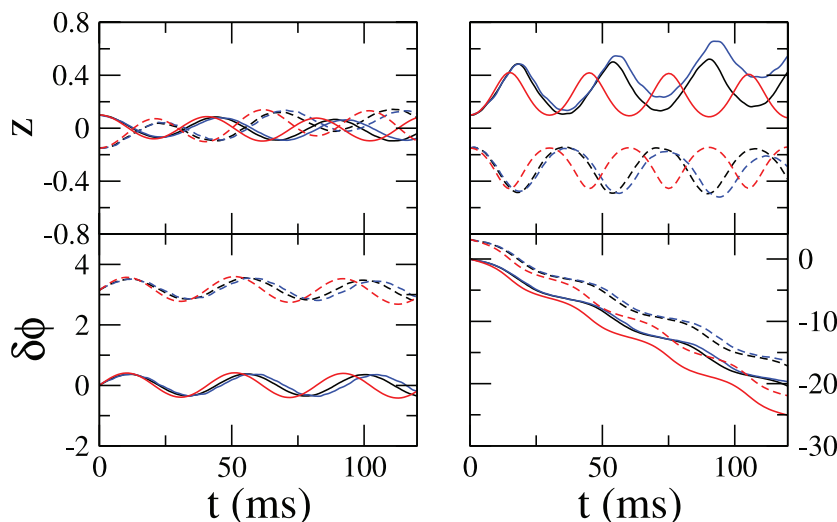
Figure 16. Two simulations with the same initial conditions, $z_a(0) = 0.1$, $z_b(0) = -0.15$, $\delta\phi_a(0) = 0$ and $\delta\phi_b(0) = \pi$ but with different compositions of the mixture. The case on the left has $f_b = 0.2$, while the case on the right $f_b = 0.8$. The blue lines are obtained by means of a full GP3D, the black lines are the NPSE results and the red lines are the I2M results. Solid and dashed lines correspond to the a and b components, respectively.

difference oscillates with its characteristic phase shift of $\pi/2$ with respect to the imbalance (lower panel). The phase of the a component oscillates around $\delta\phi_a = 0$, while $\delta\phi_b$ oscillates around $\delta\phi_b = \pi$.

A completely different picture emerges when the fraction of atoms in both components is exchanged, $f_a = 0.2 < 0.43$ (right panels), with most of the atoms populating the b component. In this case, the oscillation amplitude is large, both components remain trapped on their original sides and the phase difference becomes unbounded. This should be considered as a genuine effect of the binary mixture as each component follows a running phase mode on each side of the potential barrier.

The comparison between the NPSE and the GP3D is very satisfactory. The NPSE captures almost completely the dynamics up to times of 100 ms. In all cases, the NPSE reproduces correctly both the phase difference and population imbalance. The only sizeable discrepancies occur for times $\gtrsim 80$ ms in the run without equilibrium point (right panel).

The I2M gives a good qualitative picture of both cases but fails to provide predictions as accurate as the NPSE, as happened in the scalar case; see for instance figures 8 and 10. In particular the predicted periods of oscillation are much longer than the actual ones.

An example of simulations around non-trivial equilibrium points is presented in figure 17. As explained previously, these involve very large and opposite initial population imbalances for both components. In figure 17, we consider a case with initial conditions very close to the predicted equilibrium point using the standard two-mode, and described in figure 11, $z_a(0) = -0.78$, and $z_b(0) = 0.99$, with $f_a = 0.1$. Also in the same figure, we consider a similar run but with $f_a = 0.9$. In both cases, the NPSE and GP3D predict very similar dynamics. These simulations will be discussed again in section 6.5 as they exhibit effects that clearly go beyond a two-mode approximation.
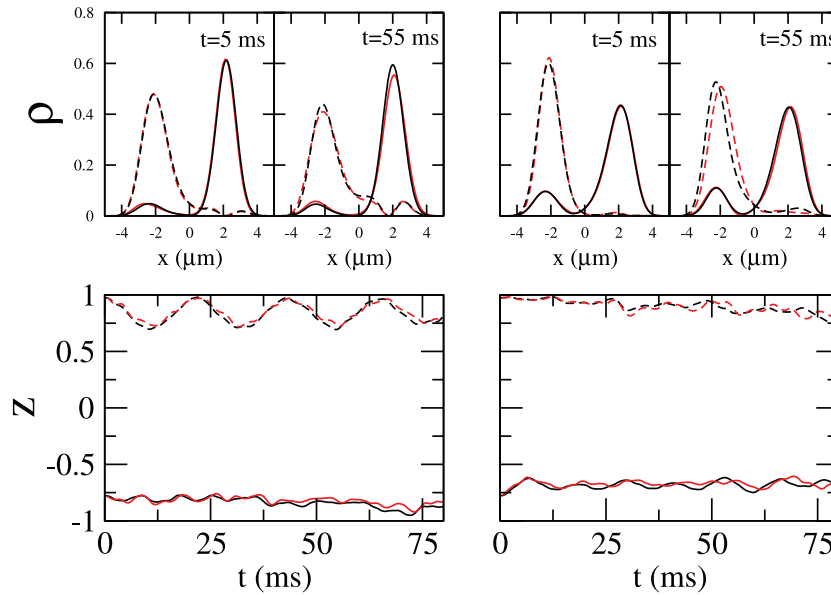
Figure 17. Two simulations with the same initial conditions, $z_a(0) = -0.78$, $z_b(0) = 0.99$, $\delta\phi_a = 0$ and $\delta\phi_b = \pi$, but with different compositions. The case on the left has $f_a = 0.1$, while the case on the right has $f_a = 0.9$. The red lines are obtained by means of a full GP3D, while the black lines are the NPSE results. Solid and dashed lines correspond to the a and b components, respectively.

6.4. Small oscillations around $z^0_{a,b}$ and $\delta\phi^0_{a,b} = \pi$

The trivial equilibrium point is not stable in the considered conditions as seen in figure 11. The non-trivial one, however, is only attainable if extremely imbalanced configurations for both components are considered. This case would correspond essentially to having both components in a π mode state, which in our conditions only exists for $z \sim 1$ as can be seen in the blue spots in panel (c) of figure 4. In figure 18, we present two simulations with different initial conditions. First, we consider a simulation with $z_a(0) = 0.4$ and $z_b(0) = -0.2$, with $f_a = 0.9$. The behavior is understood in simple terms; the most populated component remains self-trapped, while the other component is forced by the other one. The phase evolves unbounded. The figure again contains GP3D and NPSE simulations.

The second simulation (right panels) is closer to a non-trivial equilibrium point, we consider $z_a(0) = 0.9$ and $z_b(0) = 0.85$ with $f_a = 0.9$. In this case, both components remain self-trapped, the phase difference is unbounded, but we do not get the expected behavior of two π modes because the initial imbalances are not close enough to $z^0 \sim 1$.

6.5. Effects beyond two-mode

Most of the dynamics described in the previous sections can to a large extent be understood within the two-mode models developed in section 3. There are, however, a number of situations where the two-mode fails. Some are a direct consequence of having two components evolving in the same double-well potential; others are due to having initial configurations, mostly with large initial imbalances, producing situations where the atom–atom interaction energy per atom is comparable to the gap between the first excited state and the second/third excited states.
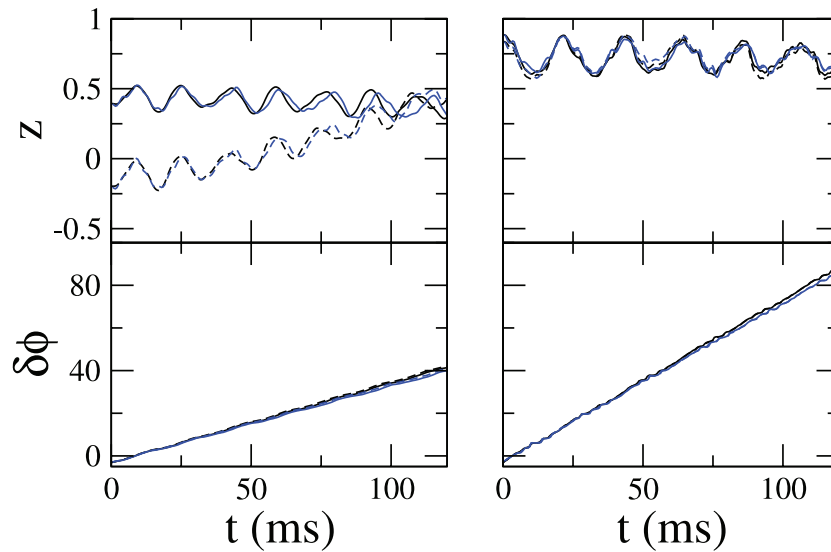
Figure 18. Two simulations corresponding to (left) $z_a(0) = 0.4$, $z_b(0) = -0.2$, $\delta\phi_a(0) = \pi$, $\delta\phi_b(0) = \pi$ and $f_a = 0.9$ and (right) $z_a(0) = 0.9$, $z_b(0) = 0.85$, $\delta\phi_a(0) = \pi$, $\delta\phi_b(0) = \pi$ and $f_a = 0.9$. The blue lines are obtained by means of a full GP3D while the black lines are the NPSE results. Solid and dashed lines correspond to the a and b components, respectively.

We can distinguish two different cases: (i) involving excitations along the coordinate that contains the barrier and (ii) involving excitations of the transversal coordinates.

An example of (i) is seen in figure 17. There, as clearly seen in the density profiles along the x-direction, the two-mode approximation is clearly not valid. The simplest way of seeing this is by noting the zero in the density of one of the components at $x \sim 2\,\mu$m. This effect beyond two-mode is well taken care of by the NPSE, which reproduces the density profile quite well during most of the time evolution considered in the simulation. Thus, the excitations of higher modes along the direction that has not been integrated out in the 1D reduction do not pose a great difficulty to the 1D reductions.

The second type, (b), of effects beyond two-mode involve excitations of the transverse components. These effects are present in any binary mixture calculation whenever the intra- and inter-species interactions are not equal. To enhance this effect, and also to explore the interesting symmetry breaking phenomena described in [30], we consider a case with $g_{aa} = g_{bb}$, but with $g_{ab} = g_{ba} = 2.3g_{aa}$. Therefore, now the inter-species interaction strength is larger than the intra-species one. The two-mode prediction for this case, S2M, which was analyzed in [30] shows a large symmetry breaking pattern during the time evolution of the system. In figure 19, we consider a full GP3D simulation of a representative example with $z_a(0) = -0.2$, $z_b(0) = 0.1$, $\delta\phi_a(0) = \delta\phi_b(0) = 0$ and $f_a = 0.7$.

The qualitative prediction of the I2M also shows symmetry breaking, and the two components separate from each other and mostly concentrate on one of the wells as time evolves. But, as can be seen in the 3D depictions of $\rho(x, y; t)$ at three different times, the evolution of the system departs, almost from the beginning, from the two-mode. At $t = 1$ ms we have the density distributions of each component corresponding to a small initial imbalance. Then at $t = 11$ ms, we can already see that the most populated component is expelling the other
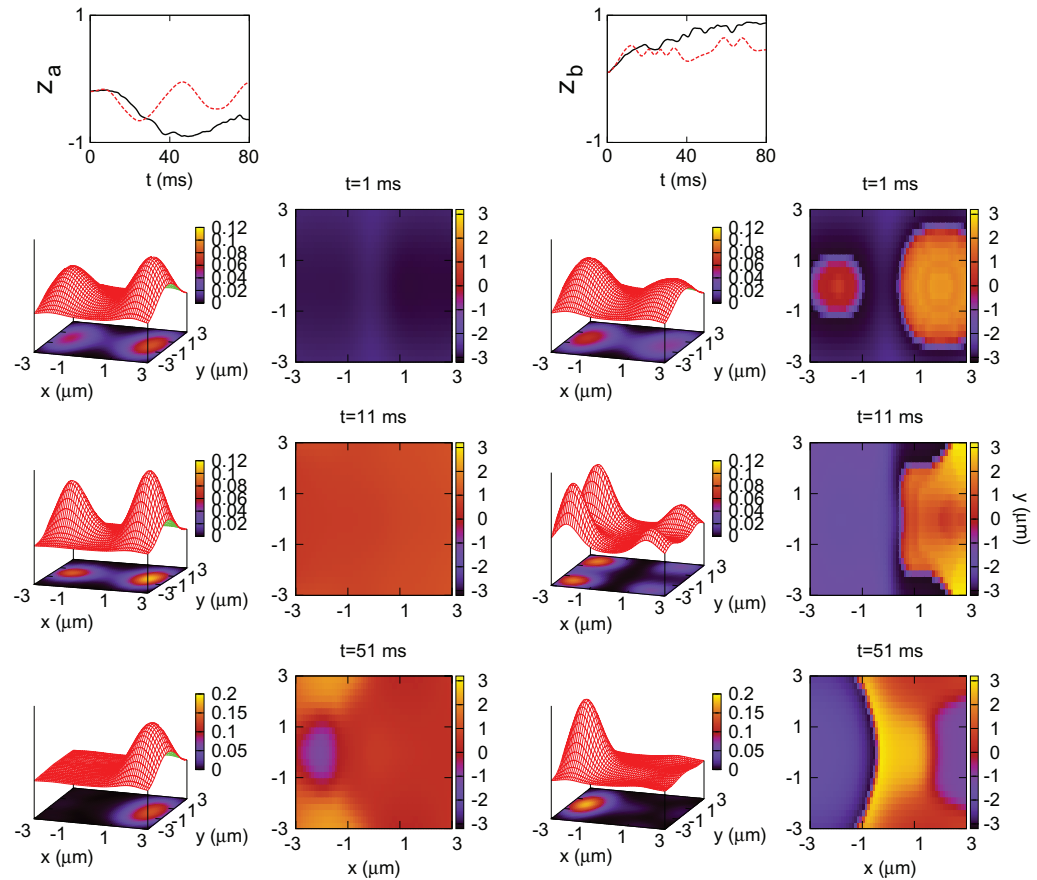
Figure 19. Full GP3D calculations of the dynamics of a binary mixture with $z_a(0) = -0.2$, $z_b(0) = 0.1$, $\delta\phi_a(0) = 0$, $\delta\phi_b(0) = 0$, $f_a = 0.7$ and $f_b = 0.3$. As explained in the text in this case, $g_{aa} = g_{bb}$ and $g_{ab} = 2.3g_{aa}$. The upper two plots depict $z_a(t)$ (left) and $z_b(t)$ (right). Then each row contains, from left to right, 3D depictions complemented by contour plots of $\rho_a(x, y; t)$, a contour plot of the averaged phase $\phi_a(x, y; t)$, 3D depictions complemented by contour plots of $\rho_b(x, y; t)$ and a contour plot of the averaged phase $\phi_b(x, y; t)$. Each row corresponds to a different time, 1 ms (upper), 11 ms (middle) and 51 ms (lower), respectively. In all cases, solid black lines are computed with GP3D and dashed red ones with I2M.

one from the minima of the potential. This fact can be appreciated as a four peaked distribution, $\rho_b(x, y; t)$. After that, each of the components starts to accumulate on their original sides following qualitatively the prediction of the I2M and thus presenting the symmetry breaking pattern discussed in [30]. The two-mode approximation is in this case broken for a short period of time, when the first modes along the transverse directions are excited due to the large inter-species interaction.

7. Conclusions

We have presented a thorough investigation of the mean-field dynamics of a binary mixture of BECs trapped in a double-well potential. As explained in the introduction, we have considered

systems with a large enough number of atoms and initial configurations of mean-field type, so that the use of mean-field approximations is justified.

The rich dynamical regimes that take place in binary mixtures, like double self-trapped modes, Josephson oscillations, or zero and π bound phase modes, have been scrutinized by performing full GP3D simulations covering all the relevant initial conditions. The 3D numerical solutions of the GP equations have been used to critically discuss the validity of the most common 1D reductions of the GP equations, GP1D and NPSE, and the often employed simple two-mode reductions, S2M and I2M.

The full 3D solutions of the binary mixture have been shown to have a large amount of phase coherence and localization at each side of the potential barrier for both components, predicting a dynamics that is mostly bi-modal. This feature permits us to speak of BECs on each side of the barrier, where the atoms mostly share a common phase, and to support the use of two-mode approximations, whose analytical solutions allow us to gain physical insight into the problem.

To fix the conditions of the dynamics, we have focused on one particular setup that corresponds to a natural extension of the experiments reported in [4]: the case of a binary mixture made by populating two of the Zeeman states of an $F = 1$ ^{87}Rb condensate. As discussed in the present paper, this setup already allows us to observe and characterize a large variety of phenomena that are genuine of the binary mixture, e.g. anti-Josephson oscillations in highly polarized cases, long Rabi-like oscillating modes, zero- and π-locked modes, etc.

For the sake of completeness and to better frame the physics of the binary mixture, we have provided a detailed description of the single component dynamics, with explicit expressions for all the commonly employed approximations to the 3D mean field GP equation. The natural extension of the latter to the binary mixture, i.e. S2M and I2M equations and 1D reductions, has been consistently derived providing a self-contained reference, easy to read, with all the relevant formulae used in the paper.

The standard two-mode model, with its microscopic parameters computed with the GP3D, has been used to reexamine the existence and stability of the different regimes that can occur in both single component and binary mixture condensates, describing the Josephson oscillations and the MQST, including running phase modes and zero- and π-modes.

The comparisons between the two-mode models and the numerical solutions of the GP3D show excellent agreement for conditions close to the stable stationary regimes predicted by the two-mode models. As we depart from those stable points, the S2M fails to show quantitative agreement with the results obtained with the GP3D equations. The range of validity of the I2M is much larger, fully capturing the dynamics of single and binary mixtures for a larger set of initial conditions.

The two most commonly employed dimensional reductions of the GP3D, the GP1D and NPSE, have been shown to differ substantially from each other, with the NPSE being clearly in much better agreement with the original 3D dynamics in a broader set of conditions. In general, the GP1D describes essentially the correct physics but quantitatively far from the GP3D predictions. Also, for self-trapped cases already in the single component case, it departs from the two-mode behavior earlier than the GP3D or the NPSE. The agreement between the NPSE and the full 3D dynamics is astonishingly good both for single component and the considered binary mixtures, where the intra- and inter-species are very similar and the NPSE equations are particularly easy to handle. This agreement is not only seen on fully integrated magnitudes, for

instance population imbalances, but also on the density profiles predicted along the direction hosting the barrier.

We have also considered two situations where the two-mode approximation fails. This is naturally due to the excitation of higher modes. Two different cases have been described: firstly, the excitation of modes in the direction of the barrier and, secondly, excitation of modes in the transverse direction. The NPSE has been shown to capture perfectly the excitations along the barrier direction, reproducing the integrated density profiles obtained with the GP3D. The second case has been studied in a simulation performed with different intra- and inter-species, which can be achieved in principle experimentally through Feshbach resonance modulation of the scattering lengths. In this case, the dynamics of the less populated component on each side of the trap departs notably from the two-mode with clear excitations of transverse modes, seen already in the density profiles along a transverse direction.

This paper is intended both to motivate the experimental effort to study binary mixtures of BECs, where we have shown that a large variety of phenomena related to phase coherence and localization can be observed, and to serve as a tool in the analysis of such experiments providing a concise and self-contained derivation of the most commonly used models.

Acknowledgments

References

[1] Leggett A J 2001 *Rev. Mod. Phys.* **73** 307
[2] Pitaevskii L and Stringari S 2003 *Bose–Einstein Condensation* (Oxford: Oxford University Press)
[3] Andrews M R, Townsend C G, Miesner H-J, Durfee D S, Kurn D M and Ketterle W 1997 *Science* **275** 637
[4] Albiez M, Gati R, Fölling J, Hunsmann S, Cristiani M and Oberthaler M K 2005 *Phys. Rev. Lett.* **95** 010402
[5] Levy S, Lahoud E, Shomroni I and Steinhauer J 2007 *Nature* **449** 579
[6] Zibold T, Nicklas E, Gross C and Oberthaler M K 2010 *Phys. Rev. Lett.* **105** 204101
[7] Smerzi A, Fantoni S, Giovanazzi S and Shenoy S R 1997 *Phys. Rev. Lett.* **79** 4950
[8] Milburn G J, Corney J, Wright E M and Walls D F 1997 *Phys. Rev.* A **55** 4318
[9] Raghavan S, Smerzi A, Fantoni S and Shenoy S R 1999 *Phys. Rev.* A **59** 620
[10] Ostrovskaya E A, Kivshar Y S, Lisak M, Hall B, Cattani F and Anderson D 2000 *Phys. Rev.* A **61** 031601
[11] Giovanazzi S, Smerzi A and Fantoni S 2000 *Phys. Rev. Lett.* **84** 4521
[12] Smerzi A and Trombettoni A 2003 *Phys. Rev.* A **68** 023613
[13] Tonel A P, Foerster A and Links J 2005 *J. Phys. A: Math. Gen.* **38** 1235
[14] Ananikian D and Bergeman T 2006 *Phys. Rev.* A **73** 013604
[15] Gati R and Oberthaler M K 2007 *J. Phys. B: At. Mol. Opt. Phys.* **40** R61
[16] Jääskeläinen M and Meystre P 2005 *Phys. Rev.* A **71** 043603
   Jääskeläinen M and Meystre P 2006 *Phys. Rev.* A **73** 013602
[17] Cirac J I, Lewenstein M, Molmer K and Zoller P 1998 *Phys. Rev.* A **57** 1208
[18] Javanainen J and Ivanov Y M 1999 *Phys. Rev.* A **60** 2351

IOP Institute of Physics Φ DEUTSCHE PHYSIKALISCHE GESELLSCHAFT

[19] Ziń P, Chwedeńczuk J, Oleś B, Sacha K and Trippenbach M 2008 *Eur. Phys. Lett.* **83** 64007
[20] Sakmann K, Streltsov A I, Alon O E and Cederbaum L S 2009 *Phys. Rev. Lett.* **103** 220601
[21] Juliá-Díaz B, Dagnino D, Lewenstein M, Martorell J and Polls A 2010 *Phys. Rev.* A **81** 023615
[22] Juliá-Díaz B, Martorell J and Polls A 2010 *Phys. Rev.* A **81** 063625
[23] Carr L D, Dounas-Frazer D R and Garcia-March M A 2010 *Europhys. Lett.* **90** 10005
[24] Boukobza E, Chuchem M, Cohen D and Vardi A 2009 *Phys. Rev. Lett.* **102** 180403
[25] Albiez M 2005 *PhD Thesis* University of Heidelberg
[26] Salasnich L, Parola A and Reatto L 2002 *Phys. Rev.* A **65** 043614
[27] Ashab S and Lobo C 2002 *Phys. Rev.* A **66** 013609
[28] Ng H T, Law C K and Leung P T 2003 *Phys. Rev.* A **68** 013604
     Wen L and Li J 2007 *Phys. Lett.* A **369** 307
[29] Xu X-Q, Lu L-H and Li Y-Q 2008 *Phys. Rev.* A **78** 043609
[30] Satija I I, Balakrishnan R, Naudus P, Heward J, Edwards M and Clark C W 2009 *Phys. Rev.* A **79** 033616
[31] Mazzarella G, Moratti M, Salasnich L, Salerno M and Toigo F 2010 *J. Phys. B: At. Mol. Opt. Phys.* **43** 065303
[32] Sun B and Pindzola M S 2009 *Phys. Rev.* A **80** 033616
[33] Naddeo A and Citro R 2010 *J. Phys. B: At. Mol. Opt. Phys.* **43** 135302
[34] Mazzarella G, Moratti M, Salasnich L and Toigo F 2010 *J. Phys. B: At. Mol. Opt. Phys.* **43** 065303
[35] Wang C, Kevrekidis P G, Whittaker N and Malomed B A 2008 *Physica* D **327** 2922
[36] Juliá-Díaz B, Guilleumas M, Lewenstein M, Polls A and Sanpera A 2009 *Phys. Rev.* A **80** 023616
[37] Wang W 2009 *J. Phys. Soc. Japan* **78** 094002
[38] Pu H, Zhang W P and Meystre P 2002 *Phys. Rev. Lett.* **89** 090401
     M̈ustecaplioglu O E, Zhang W and You L 2007 *Phys. Rev.* A **75** 023605
[39] Juliá-Díaz B, Melé-Messeguer M, Guilleumas M and Polls A 2009 *Phys. Rev.* A **80** 043622
[40] Oberthaler M 2009 private communication
[41] Olshanii M 1998 *Phys. Rev. Lett.* **81** 938941
[42] Zhang W and You L 2005 *Phys. Rev.* A **71** 025603
[43] Salasnich L and Malomed B A 2006 *Phys. Rev.* A **74** 053610
[44] Juliá-Díaz B, Martorell J, Mele-Messeguer M and Polls A 2010 *Phys. Rev.* A **82** 063626
[45] Ho T-L 1998 *Phys. Rev. Lett.* **81** 742
     Ohmi T and Machida K 1998 *J. Phys. Soc. Japan* **67** 1822
     Moreno-Cardoner M, Mur-Petit J, Guilleumas M, Polls A, Sanpera A and Lewenstein M 2007 *Phys. Rev. Lett.* **99** 020404
[46] van Kempen E G M, Kokkelmans S J J M F, Heinzen D J and Verhaar B J 2002 *Phys. Rev. Lett.* **88** 093201